AGU100 ADVANCING EARTH AND SPACE SCIENCE

Geochemistry, Geophysics, Geosystems

RESEARCH ARTICLE
10.1029/2018GC007978

Key Points:
- Tomographic imaging reveals three-dimensional seismic structure and physical properties of crust and mantle beneath an entire ridge segment
- Segment-scale seismic structure and recent diking events are inconsistent with centralized magma supply
- Skew between the mantle and crustal magmatic systems governs magmatic and hydrothermal activity at mid-ocean ridges

Supporting Information:
- Supporting Information S1

Correspondence to:
G. M. Arnoux,
arnoux@uoregon.edu

Citation:
Arnoux, G. M., Toomey, D. R., Hooft, E. E. E., & Wilcock, W. S. D. (2019). Seismic imaging and physical properties of the Endeavour segment: Evidence that skew between mantle and crustal magmatic systems governs spreading center processes. *Geochemistry, Geophysics, Geosystems*, *20*, 1319–1339. https://doi.org/10.1029/2018GC007978

Received 20 SEP 2018
Accepted 28 JAN 2019
Accepted article online 3 FEB 2019
Published online 7 MAR 2019

Seismic Imaging and Physical Properties of the Endeavour Segment: Evidence that Skew Between Mantle and Crustal Magmatic Systems Governs Spreading Center Processes

G. M. Arnoux[1], D. R. Toomey[1], E. E. E. Hooft[1], and W. S. D. Wilcock[2]

[1]Department of Earth Sciences, University of Oregon, Eugene, OR, USA, [2]School of Oceanography, University of Washington, Seattle, WA, USA

Abstract We invert *Pg*, *PmP*, and *Pn* traveltimes from an active-source, multiscale tomography experiment to constrain the three-dimensional isotropic and anisotropic *P* wave velocity structure of the topmost oceanic mantle and crust and crustal thickness variations beneath the entire Endeavour segment of the Juan de Fuca Ridge. The isotropic velocity structure is characterized by a semicontinuous, narrow (5-km-wide) crustal low-velocity volume that tracks the sinuous ridge axis. Across the Moho, the low-velocity volume abruptly broadens to approximately 20 km in width and displays a north-south linear trend that connects the two overlapping spreading centers bounding the segment. From the seismic results, we estimate the thermal structure and melt distribution beneath the Endeavour segment. The thermal structure indicates that the observed skew, or lateral offset, between the crustal and mantle magmatic systems is a consequence of differences in mechanisms of heat transfer at crustal and mantle depths, with the crust and mantle dominated by advection and conduction, respectively. Melt volume estimates exhibit significant along-axis variations that coincide with the observed skew between the mantle and crustal magmatic systems, with sites of enhanced crustal melt volumes and vigorous hydrothermal activity corresponding to regions where the mantle and crustal magmatic systems are vertically aligned. These results contradict models of ridge segmentation that predict enhanced and reduced melt supply beneath the segment center and ends, respectively. Our results instead support a model in which segment-scale skew between the crustal and mantle magmatic systems governs magmatic and hydrothermal processes at mid-ocean ridges.

1. Introduction

The global mid-ocean ridge system accounts for ~75% of Earth's annual magma budget (Crisp, 1984). Magmatic systems beneath spreading centers drive high- and low-temperature hydrothermal activity that modulates the long-term chemistry of the ocean, hydrates the crust and mantle, supports novel ecosystems, and deposits valuable mineral resources. The fundamental unit of the global mid-ocean ridge system is referred to as a ridge segment. Within a single ridge segment there are systematic variations in tectonic, volcanic, and hydrothermal processes (Kent et al., 2000; Langmuir et al., 1986; Macdonald et al., 1988). Understanding how mass and energy are transferred within a ridge segment requires mapping mantle and crustal magmatic systems and their relationship to hydrothermal and tectonic processes. Maps of the three-dimensional seismic structure can constrain the size, shape, and location of magma reservoirs, the connections between magmatic and hydrothermal processes, and be used to infer the thermal structure (Carbotte et al., 2012, 2013; Detrick et al., 1987; Dunn et al., 2000, 2013; Kent et al., 1993, 2000; Seher et al., 2010; West et al., 2001).

Much of what we know regarding mid-ocean ridge crustal magmatic systems is derived from seismic studies of the fast-spreading East Pacific Rise (EPR; Carbotte et al., 2013; Dunn et al., 2000; Goss et al., 2010). In the cross-axis direction, EPR magmatic systems consist of a steep-sided mush zone that is often capped by a narrow, thin melt lens (Dunn et al., 2000). In the rise-parallel direction, EPR crustal magmatic systems are to first-order, two-dimensional features with predominantly vertical flow, though there are subtle structures that vary along-axis at a variety of scales (e.g., Carbotte et al., 2013; Hooft et al., 1997; Kent et al., 1993, 2000; Toomey et al., 1990; Wilcock et al., 1993). To what degree crustal magmatic systems at other spreading rate ridges resemble their fast-spreading counterparts is not well known.

10.1029/2018GC007978

At the intermediate-spreading, back-arc Eastern Lau Spreading Center, a narrow, seismic low-velocity volume (LVV) is imaged into the mid-crust beneath all surveyed ridge segments (Dunn et al., 2013). At the intermediate-spreading Juan de Fuca Ridge (JdFR), an axial magma lens (AML) reflector underlies most ridge segments, though it is less laterally continuous and its along-axis depth variation is more pronounced than that at the EPR (Carbotte et al., 2006, 2008; Van Ark et al., 2007). This reflector may overlie a lower crustal mush zone that is comparable to the EPR, with steep sides that are consistent with rapid convective cooling at lower crustal depths (e.g., Hasenclever et al., 2014; Henstock et al., 1993), and with a mush zone that extends to the Moho and varies slowly along axis, as one might expect for largely two-dimensional (vertical) melt transport through the lower crust (Carbotte et al., 2013; Sinton & Detrick, 1992; Toomey et al., 1990). Alternatively, the lower crustal mush zone at intermediate-spreading ridges may be more three-dimensional, with more along-axis heterogeneities, and consistent with focused melt transport through the lower crust, along-axis transport of magma at midcrustal depths, and uneven rates of hydrothermal cooling. Such along-axis variations in melt transport could have significant implications for the observed segmentation of mid-ocean ridges, defined by systematic along-axis variations in tectonic and magmatic processes.

The origin of mid-ocean ridge segmentation is commonly attributed to three-dimensional mantle upwelling (Macdonald et al., 1988, 1991; Schouten et al., 1985). In this view, the supply of magma from the mantle is enhanced beneath intrasegment highs (Francheteau & Ballard, 1983; Macdonald et al., 1988; Whitehead et al., 1984). This model would thus predict thickened crust beneath axial depth minima or segment-scale redistribution of magma. Crustal thickness at the 9°N segment of the EPR, however, does not correlate with ridge-crest depth (Barth & Mutter, 1996; Canales et al., 2003; Toomey & Hooft, 2008). The thickest crust is located in the wake of the 9°03′N overlapping spreading center (OSC), whereas thinner crust underlies the segment near 10°N where the ridge crest is shallower (Barth & Mutter, 1996; Canales et al., 2003). Additional observations of segment-scale variations in crustal thickness are required to further assess this hypothesis.

An alternative model for the origin of ridge segmentation is that of skew between the axes of mantle upwelling and plate spreading. At shallow mantle depths, results from the EPR (Toomey et al., 2007; Toomey & Hooft, 2008) and Endeavour segment of the JdFR (VanderBeek et al., 2016) suggest that skew, or misalignment between tectonic rifting, mantle divergence, and segment-scale delivery of mantle melt to the crust, governs along-axis variations in ridge-crest volcanic, hydrothermal, and tectonic activity. In this model, axis-parallel variations in ridge processes are not simply a function of magma supply or the along-axis redistribution of magma away from a mantle source beneath the center of the ridge segment, as is predicted by the magma supply model (Bell & Buck, 1992; Macdonald et al., 1988, 1991). Rather, the cross-axis offset between the locus of mantle melt supply and the ridge axis governs along-axis variations in ridge crest processes (Toomey et al., 2007; VanderBeek et al., 2016). This model predicts frequent magma injection into the rift, frequent extrusive volcanism, and more vigorous hydrothermal venting that would shape a narrow, robust crustal magmatic system in sites of axis-centered mantle melt delivery. In contrast, sites of off-axis mantle melt delivery would have less frequent magma injection and extrusive volcanism, less intense hydrothermal activity, comparatively higher degrees of magmatic differentiation, and a weaker crustal magmatic system. To date, however, no studies have imaged the segment-scale structure of the magmatic system in its entirety, from the shallow mantle to upper crust, in regions where skewed mantle melt delivery is observed.

In this study, we utilize seismic tomographic methods to constrain the three-dimensional segment-scale variations in the isotropic and anisotropic velocity structure of the topmost mantle and crust beneath an entire ridge segment. Our results provide new insight into the thermal and magmatic structure beneath the Endeavour segment, in addition to crustal thickness variations beneath the ridge axis. We discuss the implications of our results on (i) the magma plumbing system beneath the Endeavour segment, (ii) the relationship between skewed delivery of mantle melt and the structure of the crustal magmatic system, and (iii) the relationship between crustal thickness, magma supply, and the tectonic evolution of the Endeavour segment.

2. Background

The Endeavour segment is a 90-km-long intermediate-rate spreading center (57 mm/year; DeMets et al., 2010) located on the northern end of the JdFR (Figure 1). It lies at the southern edge of the diffuse

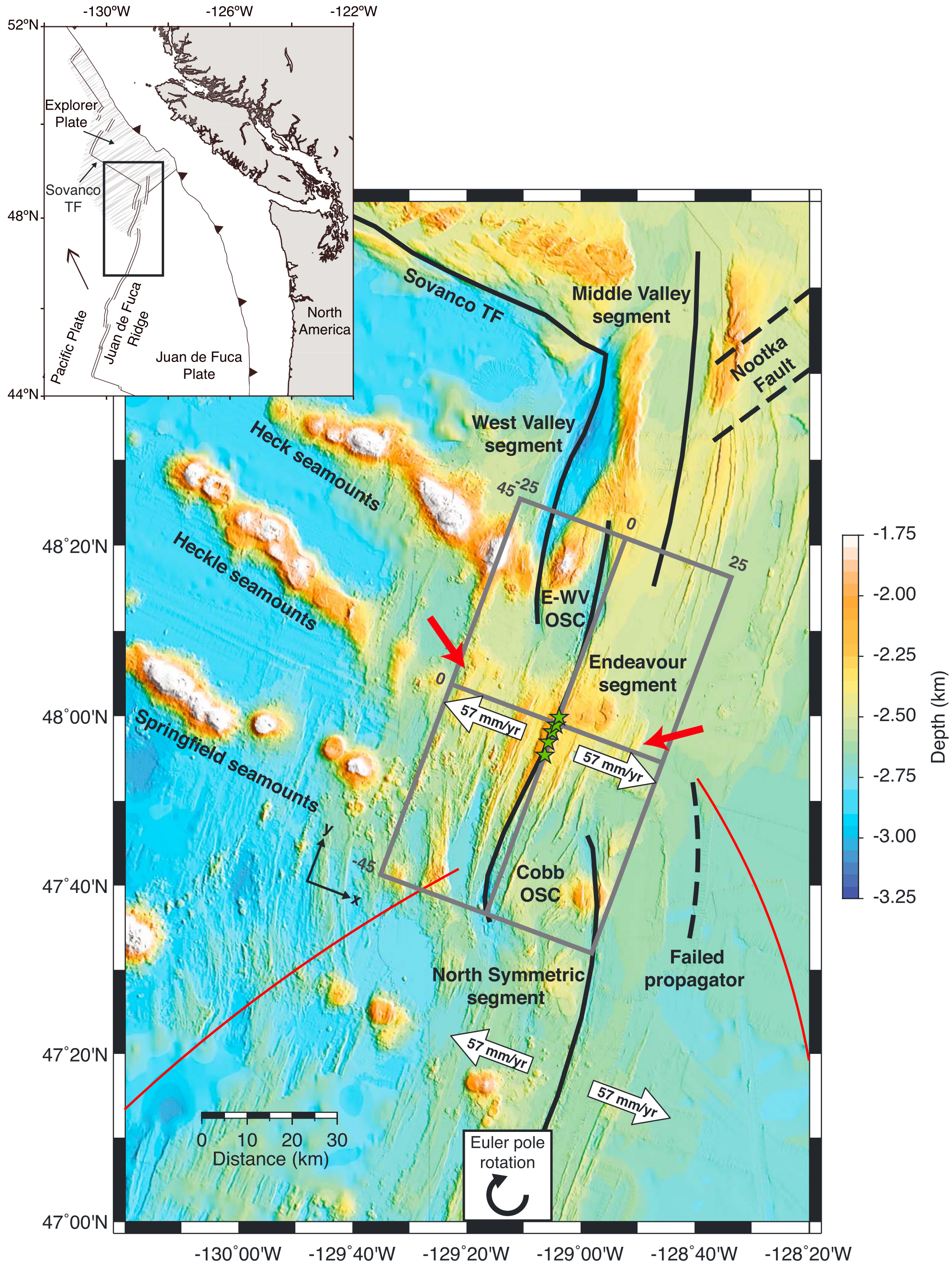

Figure 1. Bathymetric map of the Endeavour region of the Juan de Fuca Ridge showing the major tectonic features. Solid black lines demarcate plate boundaries, with transform faults (TF) and overlapping spreading centers (OSCs) labeled. The white arrows show spreading direction and full-spreading rate (Gripp & Gordon, 2002). The red arrows point to the boundaries of the axis-centered plateau discussed in text. Green stars show the location of high-temperature vent fields. Red lines indicate propagator wakes and the gray box outlines the Cartesian coordinate system, in kilometers, for the areas shown in Figures 5, 6, S7, and S8. Recent rotation in the Euler pole of the Juan de Fuca-Pacific plate system is indicated (Wilson, 1988). Top left inset, modified from Byrnes et al. (2017), shows the tectonic context of the Endeavour segment. Shown are spreading centers (double lines), transform faults (black lines), direction of ridge migration (thin arrow), the Cascadia megathrust (black line with triangles), and the diffuse Explorer plate boundary (streaked area; Dziak, 2006).

Explorer plate boundary, a deformation zone that extends to the Cobb OSC and bounds the southern end of the Endeavour segment (Figure 1; Dziak, 2006). To the north, the Endeavour segment is bounded by the Endeavour-West Valley (E-WV) OSC. The tectonic history of the Endeavour segment is dominated by a series of ridge propagation events. The Cobb OSC, which separates the Endeavour and Northern Symmetric segments by >30 km, propagated northward ~4.5 Ma (Wilson, 1993). The Endeavour segment propagated southward ~0.8 Ma, forcing retreat of the Cobb OSC to approximately 47°35′N (Shoberg et al., 1991). Propagation again reversed within the past 0.1 Ma, with the northern end of Northern Symmetric segment currently located at 47°46′N. The E-WV OSC to the north separates the Endeavour and West Valley segments by 15 km and formed within the past 0.2 Ma when the spreading center jumped from the Middle Valley segment to West Valley segment (Figure 1; Davis & Lister, 1977; Davis & Villinger, 1992).

The central portion of the Endeavour segment hosts five large hydrothermal vent fields that are spaced 2–3 km apart along the ridge axis (Figure 1; Kelley et al., 2002). These vent fields mine heat from a crustal magmatic system capped by an AML that is located 2.1–3.3 km below the seafloor and extends ~20 km along axis (Van Ark et al., 2007). The vent fields exhibit significant along-axis variability in chemistry, temperature (Butterfield et al., 1994; Kelley et al., 2002, 2012), and heat flux (Kellogg, 2011). Along-axis gradients in heat flux correlate with concentrations of seismicity related to recent magma chamber inflation (Wilcock et al., 2009) and imaged variations in low velocities above and beneath the AML (Arnoux et al., 2017), with the most intense seismicity and lowest velocities occurring beneath the High Rise and Main Endeavour vent fields, the vent fields with the highest heat fluxes (Kellogg, 2011).

A 6-year-long, noneruptive spreading event ruptured the Endeavour from 1999 to 2005 (Weekly et al., 2013). The initiation and termination of the spreading episode were defined by large seismic swarms linked to intrusive volcanism and lateral dike propagation (Bohnenstiehl et al., 2004; Hooft et al., 2010). During the 1999 swarm, the initial pulse of seismicity was distributed along-axis in the region of the imaged AML and subsequently migrated ~12 km south along the Endeavour segment (Bohnenstiehl et al., 2004). The 2005 seismic sequence, marking the termination of the spreading episode, initiated at the northern end of the Endeavour segment near the E-WV OSC and progressed 20 km south toward the segment center over the course of 5 days (Hooft et al., 2010). Smaller dike intrusions on the propagating tip of the West Valley segment were also detected during the 2005 swarm (Hooft et al., 2010; Weekly et al., 2013).

The axial high at Endeavour is located within a 40-km-wide plateau that is elevated 300 m relative to the rest of the segment (Figure 1; Carbotte et al., 2008). The plateau is underlain by thickened crust, on the order 0.5–1 km thicker than average flank crust (Carbotte et al., 2008; Soule et al., 2016). It has been postulated that the plateau is the result of enhanced crustal production due to the interaction of the Endeavour segment with a shallow mantle thermal anomaly related to the Heckle Seamount chain (Carbotte et al., 2008). Alternatively, the plateau may be the product of the propagation history of the Cobb OSC, in which the southward migration of the Endeavour segment 0.71 Ma generated thicker crust by tapping melt pooled beneath the Cobb OSC (Soule et al., 2016).

3. Experiment Geometry and Data

The seismic data were collected in 2009 during the Endeavour seismic tomography (ETOMO) experiment. The seismic experiment was comprised of 68 four-component (three orthogonal geophones and a hydrophone) ocean bottom seismometers deployed at 64 unique sites that recorded ~5,500 air gun shots from the 36 element, 6,600-in^3 air gun array of the R/V *Marcus G. Langseth* (Figure 2a). The objective of the experiment was to image the crustal and mantle structure from the segment to vent field scales (Arnoux et al., 2017; Soule et al., 2016; VanderBeek et al., 2016; Weekly et al., 2014). To accomplish this, a nested source receiver geometry was used to record data that densely sampled the crust and topmost mantle within a 90-km-by-50-km area centered on the ridge segment (Figure 2a). This nested geometry consisted of three grids: (i) the segment-scale undershoot grid designed to image the topmost mantle structure using six rise-parallel 105-km-long lines shot within 30 km of the ridge axis and two rise-perpendicular lines shot on the northern and southern margins of the experiment; (ii) the crustal grid devised to image the off-axis crustal structure and along-axis variation of the crustal magmatic system, composed of 19 shot lines spaced 1 km apart within a 20-by-60-km^2 area centered on the central plateau of the segment; and (iii) the fine-scale hydrothermal grid designed to image the detailed structure of the shallow crust beneath and near the hydrothermal vents, consisting of the densest shot-receiver distribution within the Endeavour tomography experiment with ten 20-km-long shot lines embedded within the center of the crustal grid for a net spacing of 500 m. Shot spacing along all lines was 450 m. The data have been used to constrain the isotropic and

10.1029/2018GC007978

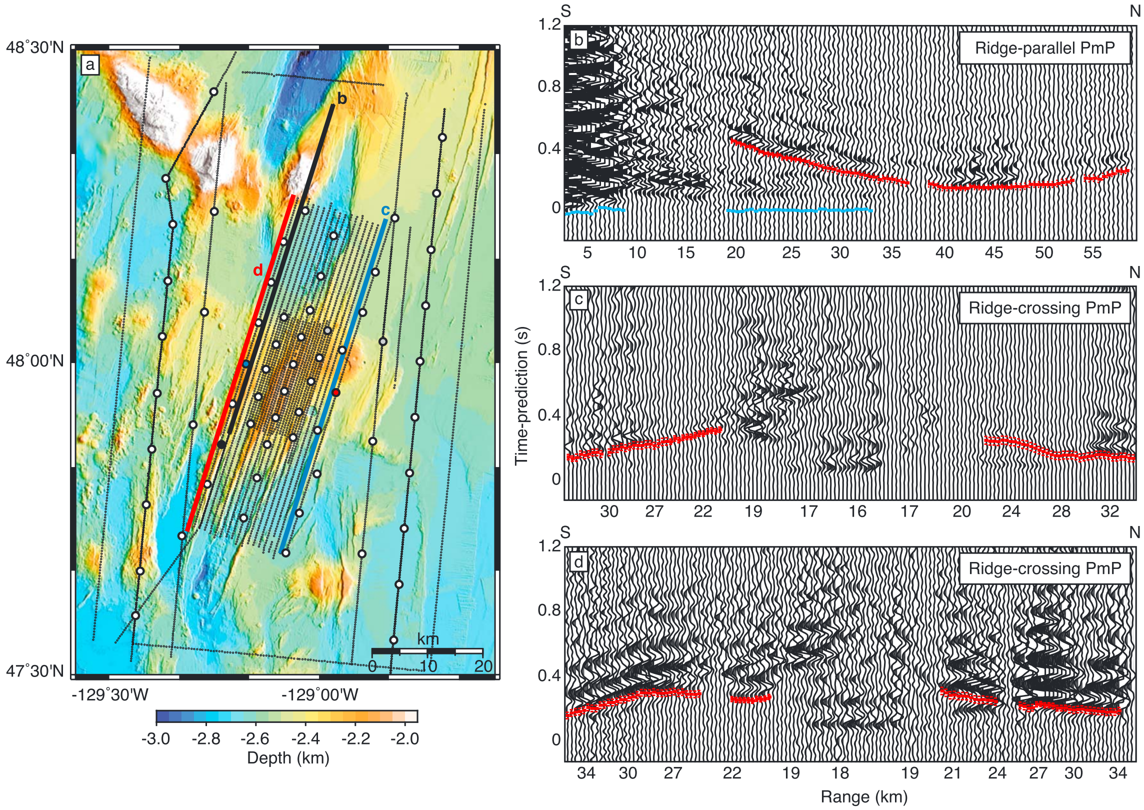

Figure 2. Geometry of the Endeavour tomography (ETOMO) experiment and example record sections. (a) Configuration of the ETOMO experiment, consisting of 68 four-component ocean bottom seismometers (white circles) that recorded ~5,500 air gun shots (black dots). Two ocean bottom seismometers did not record useable data (gray circles). The black, blue, and red circles and lines show the locations of the receivers and sources shown in (b)–(d), respectively. (b) Record section for ridge-parallel raypaths with *Pg* arrivals marked by blue lines (Weekly et al., 2014). (c and d) Record sections for ridge-crossing raypaths. Record sections show *PmP* traveltime picks (red lines) and assigned picking errors (red dashes). Traces are aligned by range of shots in kilometers. Record sections are plotted after applying a 5- to 20-Hz band-pass filter, and times are zeroed at the predicted *Pg* arrival time for the preferred model to remove complex bathymetric effects.

anisotropic *P* wave velocity structure of the upper crust (Arnoux et al., 2017; Morgan et al., 2016; Weekly et al., 2014), near-axis crustal velocity structure and thickness (Soule et al., 2016), mantle velocity and anisotropy structure (VanderBeek et al., 2016), and upper crustal Vp/Vs structure (Kim et al., 2019). Until now, the data have not been used to image the lower crustal velocity structure and crustal thickness beneath the rise axis.

Our tomographic analysis includes traveltimes from 96,155 primary crustal arrivals (*Pg*), 105,000 Moho- (*PmP*), and 12,000 mantle-turning (*Pn*) arrivals. Of the *PmP* picks included, 55,000 are ridge parallel (Figure 2b) and 50,000 are ridge crossing (Figures 2c and 2d); we detail the process of picking *PmP* arrivals in Text S1 in the supporting information and provide additional data sections in Figure S1. The root-mean-square (RMS) picking uncertainty for the entire *PmP* data set is 18.7 ms. Previous tomography studies have modeled *Pg* (Weekly et al., 2014) and *Pn* arrivals (VanderBeek et al., 2016) and 40% of the ridge-parallel *PmP* (Soule et al., 2016). No previous work has incorporated ridge-crossing *PmP* arrivals.

4. Tomographic Method

We used a three-dimensional tomographic technique to invert traveltime data to constrain isotropic slowness and seismic anisotropy within the crust and topmost mantle, in addition to Moho depth (Dunn et al., 2005; Toomey et al., 1994). The inverse technique involves computing three-dimensional seismic raypaths between sources and receivers to calculate traveltimes through a starting model. The inverse problem is linearized about this starting model to obtain a set of equations mapping model perturbations into traveltime residuals. User-prescribed values for model smoothness and variance are included via additional equations. The model is then updated with a correction calculated via a least squares procedure utilizing either a creeping or jumping inversion strategy (Shaw & Orcutt, 1985), and subsequent iterations are performed until the RMS traveltime residuals converged. Our preferred model converged to a RMS of 11 (χ^2 = 1.02), 16 (χ^2 = 0.87), and 11.2 ms (χ^2 = 1.2) for *Pg*, *PmP*, and *Pn*, respectively. A detailed description of the inversion approach is presented in Text S2.

4.1. Forward Problem

The velocity model is parameterized in terms of slowness with nodes defined on a regular grid aligned with the trend of the ridge axis. Nodes are spaced every 200 m in the *x* and *y* dimensions and 250 m in the *z* dimension. The model extends 90 km in the cross-axis direction, 120 km in the rise-parallel direction, and 11 km beneath the seafloor. The forward problem utilizes a shortest-path ray tracing method that accounts for anisotropic structure (Barclay et al., 1998) and incorporates seafloor topography by vertically shearing columns within the velocity model to follow local seafloor relief (Toomey et al., 1994). Anisotropic slowness is parameterized assuming a hexagonal symmetry system on the slowness grid:

$$u\left[\boldsymbol{r},\widehat{\boldsymbol{R}};u_{\text{iso}}(\boldsymbol{r}),a(\boldsymbol{r}),\widehat{\boldsymbol{S}}\right]=\frac{u_{\text{iso}}(\boldsymbol{r})}{1+\kappa\left[\frac{a(\boldsymbol{r})}{2}\cos(2\theta)\right]} \tag{1}$$

where $u_{\text{iso}}(\boldsymbol{r})$ is the isotropic velocity defined at nodal position $\boldsymbol{r}$, κ is a scalar that determines the symmetry system, defined as ± 1 (positive and negative for fast and slow symmetry axis in the horizontal plane, respectively), $a(\boldsymbol{r})$ is the fraction of anisotropy, defined as $(v_{\max}\text{-}v_{\min})/v_{\text{average}}$, where v is the *P* wave velocity, $\widehat{\boldsymbol{S}}$ and $\widehat{\boldsymbol{R}}$ are unit vectors along the symmetry axis and raypath, respectively, and θ is the angle between $\widehat{\boldsymbol{S}}$ and $\widehat{\boldsymbol{R}}$, such that $\cos(\theta)=\widehat{\boldsymbol{S}}\cdot\widehat{\boldsymbol{R}}$. The modification to this equation, κ, allows for the inclusion of two distinct symmetry systems of horizontal transverse isotropy (HTI) within the model space that approximate (i) fluid-filled cracks (slow symmetry axis), defined by one slow and two fast axes, and (ii) olivine-dominated peridotite (fast symmetry axis), defined by one fast and two slow axes. Crustal anisotropy is often caused by the alignment of fluid-filled cracks perpendicular to the minimum compressive stress direction, resulting in a horizontal axis of symmetry (slow direction of *P* wave propagation) that is oriented subperpendicular to the ridge axis. In this HTI medium, there are two fast axes oriented sub-parallel to the ridge axis and vertical (e.g., Barclay & Toomey, 2003). Mantle anisotropy is the result of lattice-preferred orientation of olivine crystals, in which the crystallographic *a* axis of olivine (the fast direction of *P* wave propagation) aligns parallel to the direction of maximum shear and thus tracks the mantle divergence direction (e.g., VanderBeek et al., 2016). In this HTI medium, there are two slow axes oriented subparallel to the ridge axis and vertical. We therefore define κ as a grid with the same dimensions as the slowness model with all crustal and mantle values set to -1 and $+1$, respectively. We note that the crustal HTI medium effectively decreases *PmP* traveltimes relative to either the isotropic or fast symmetry axis case, as *PmP* waves predominately propagate in the vertical dimension. As a result, accounting for upper crustal crack-induced anisotropy will yield systematically larger crustal thickness estimates.

The Moho reflection surface is defined on a separate gridded surface with the same *x* and *y* dimensions as the slowness grid, but for which the z grid points vary independently of the slowness grid (Dunn et al., 2005). If the Moho is raised or lowered within the model space during the inversion, values on the velocity grid are modified to maintain any velocity contrast associated with the interface, which is initially defined by the user and can vary during the inversion.

4.2. Inverse Problem

The inverse problem is regularized with damping and smoothing constraints requiring user-defined a priori model uncertainties and smoothing parameters that operate on perturbational models parameterized for isotropic slowness, anisotropy, and Moho depth. The perturbational models for isotropic and anisotropic slowness were composed of rectilinear grids with a horizontal spacing of 0.5 km within 10 km of the ridge, to reflect the greater number of raypaths, and 1 km elsewhere in the model space. Vertical node spacing varied to account for the decrease in raypath density with depth, with a minimum spacing of 500 m in the upper 3 km of crust and 1 km spacing below. Perturbational nodes for the Moho were spaced every 3 km to allow the Moho to smoothly vary. The inverse problem is parameterized as in Dunn et al. (2005), with the addition of κ to their equations A17 and A19, as in equation (1), to account for the two anisotropy symmetry axes. We note that this parametrization is an approximation of equation (1) because it only addresses azimuthal

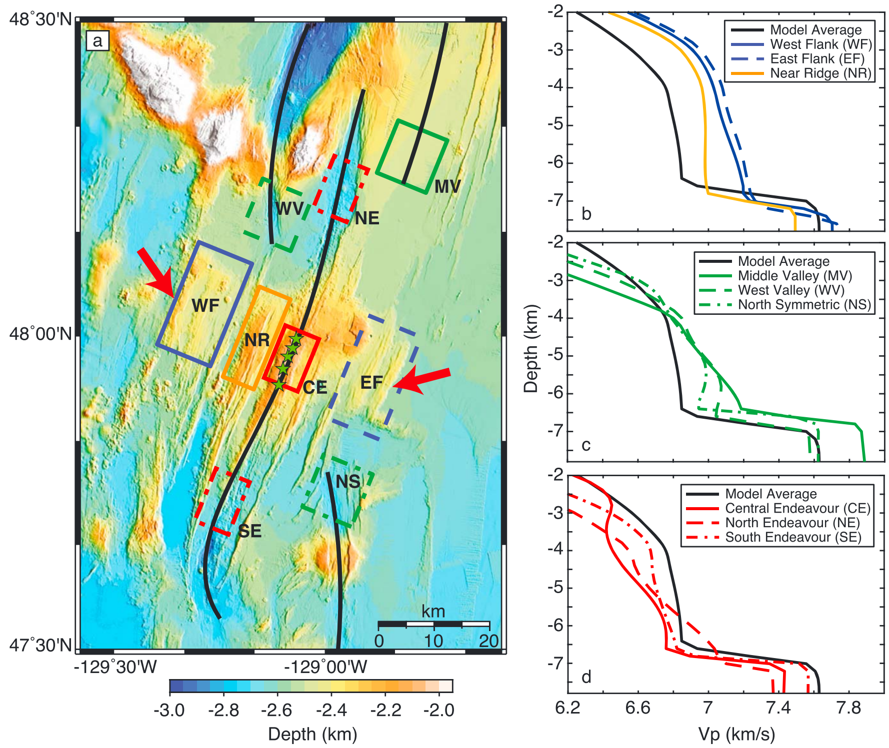

Figure 3. One-dimensional *P* wave velocity profiles. (a) Bathymetric map with regions for which average one-dimensional profiles are calculated (colored boxes); labels correspond to those shown in (b)–(d). The traces of the ridge segments are shown by black lines, axis-centered plateau boundaries by red arrows, and vent fields by green stars. (b) One-dimensional vertical profiles for the western (solid blue) and eastern flanks of the segment center (dashed blue), as well as for a region not associated with thickened ridge flank crust (solid orange). (c) Profiles for currently and formerly propagating limbs: Middle Valley (solid green), West Valley (dashed green), and North Symmetric (dotted green). (d) Profiles for the southern (dotted red), northern (dashed red), and central (solid red) portions of the Endeavour segment. The horizontal average of the isotropic component of the preferred velocity model (solid black) are shown in (b)–(d) for comparison.

anisotropy in the horizontal plane. While this approximation is exact for horizontally propagating waves, it is less accurate for diving waves. It does, however, capture the correct sign and magnitude of the partial derivatives for slowness structure, interface depth, and anisotropy, as they are controlled by the azimuth of the raypath, which changes little from iteration to iteration. Thus, because we solve the inverse problem using an iterative technique and correctly account for three-dimensional anisotropy in the forward problem, this approximation in the inverse problem is negligible.

5. Results

Previous results constrain the isotropic and anisotropic structure of the upper crust (Weekly et al., 2014) and topmost mantle (VanderBeek et al., 2016), as well as isotropic structure of off-axis lower crust and crustal thickness (Soule et al., 2016). Our study is the first to synthesize these results and provides novel constraints on the crustal velocity structure and thickness beneath and near the rise axis and the relationship between crustal and upper mantle structures along an entire ridge segment. We describe the characteristic velocity structure of different regions within the study area (Figure 3), depth variations in the velocity structure (Figure 4), and along- and cross-axis velocity variations (Figure 5). We assess the resolution of the preferred model by analyzing the spatial distribution of raypaths and conducting synthetic checkerboard tests in Text S3 and Figure S2. Additional synthetic inversions demonstrate that there is little trade-off between crustal thickness and crustal velocity (Figure S3). We also describe the mantle and crustal anisotropic structure of our preferred model in Text S2; Figures S4 and S5 show the crustal anisotropic structure of the preferred model and traveltime residuals versus azimuth for the different seismic phases, respectively.

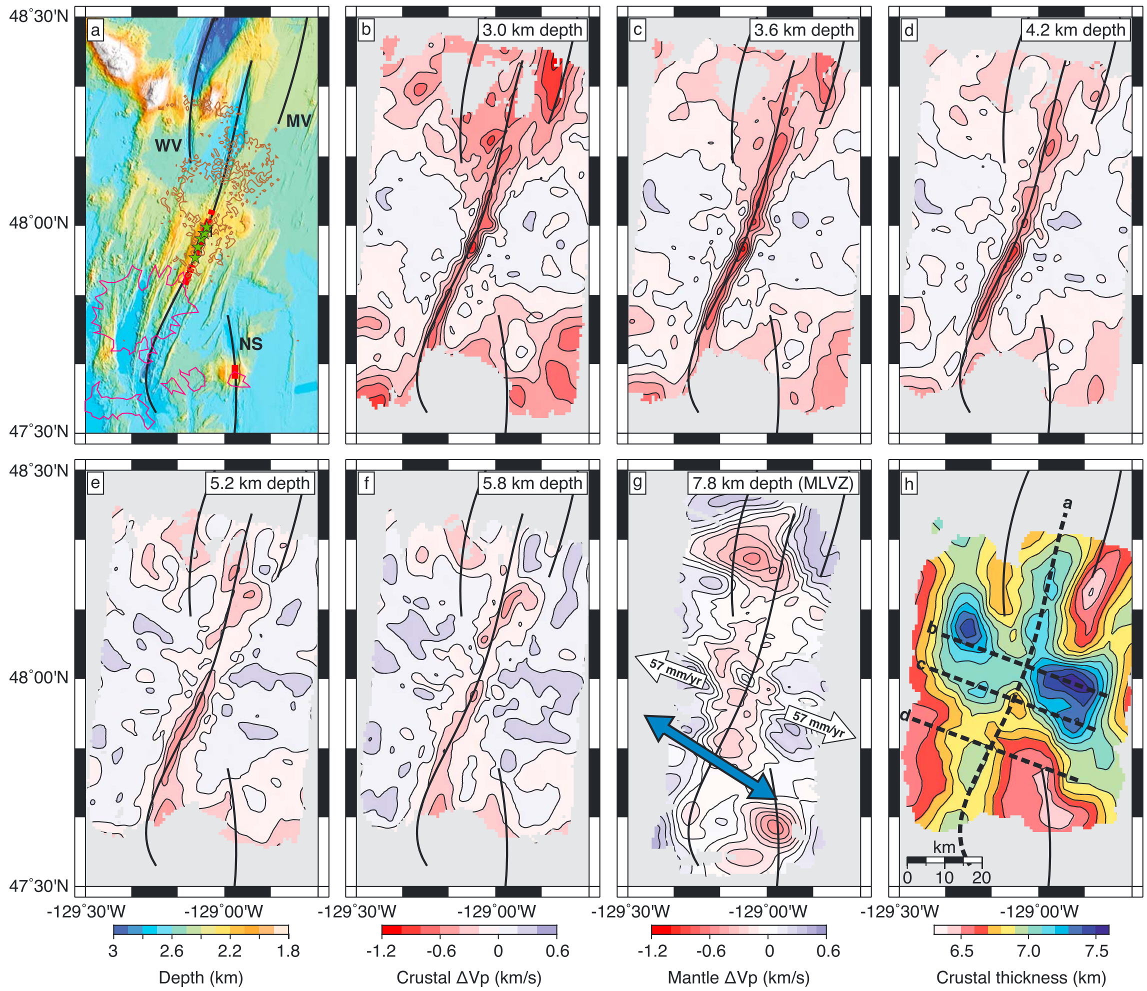

Figure 4. Comparison of bathymetry, velocity structure, and crustal thickness. (a) Bathymetry map of the Endeavour segment showing vent fields (green stars), axial magma chamber reflector (red line segments; Carbotte et al., 2012; Van Ark et al., 2007), and traces of the ridge segments (solid black lines) with West Valley (WV), Middle Valley (MV), and North Symmetric (NS) labeled. Magenta and brown contours outline regions of intense seismicity associated with the 1999 (Bohnenstiehl et al., 2004) and 2005 (Hooft et al., 2010) seismic swarms, respectively. (b–f) Map view sections through the crustal portion of the preferred velocity model at (b) 3.0-km depth, (c) 3.6-km depth, (d) 4.2-km depth, (e) 5.2-km depth, and (f) 5.8-km depth. (g) Map view section of the topmost mantle structure at 7.8-km depth. White arrows show plate spreading direction and full-spreading rate (Gripp & Gordon, 2002), and blue arrow shows azimuth of seismic anisotropy. Three-dimensional velocity perturbations are relative to the off-axis one-dimensional velocity model shown in Figure 3b (orange line). The contour interval is 0.2 km/s for (b)–(f) and 0.1 km/s for (g). (h) Segment-scale crustal thickness map. Sections (b)–(h) show plate boundaries (solid black lines) and are masked where the density of raypaths, or the derivative weight sum (Toomey & Foulger, 1989), is less than 10 (see supporting information). Dashed lines in (h) indicate locations of vertical tomographic slices shown in Figure 5. MLVZ = mantle low-velocity zone.

5.1. Mantle Velocity Structure

Velocities within the mantle are relatively low (<−0.1 km/s) along most of the Endeavour segment and similar to those of VanderBeek et al. (2016; Figure 4g). The north-south trend of the mantle low-velocity zone (MLVZ) connects the two OSCs bounding the segment and is rotated anticlockwise relative to the trend of the Endeavour segment. The trend of MLVZ, however, is subparallel to the north-south trend of the northern Juan de Fuca (JdF) plate boundary. Moreover, the MLVZ is not perpendicular to the anisotropic component of our model (blue arrow, Figure 4g), as is the case for the fast-spreading EPR (Toomey et al., 2007). The magnitude of the MLVZ is greatest beneath the two OSCs, though three distinct low-velocity minima punctuate the MLVZ beneath the central Endeavour segment (Figure 4g). The cross-axis offset of the MLVZ minima with respect to the ridge axis, or skew, varies along the segment. The two southern anomalies roughly align with the ridge axis, though the southernmost anomaly is slightly offset ~2 km to the east. Conversely, the northern minimum is offset to the west of the ridge axis by ~10 km. Of note is

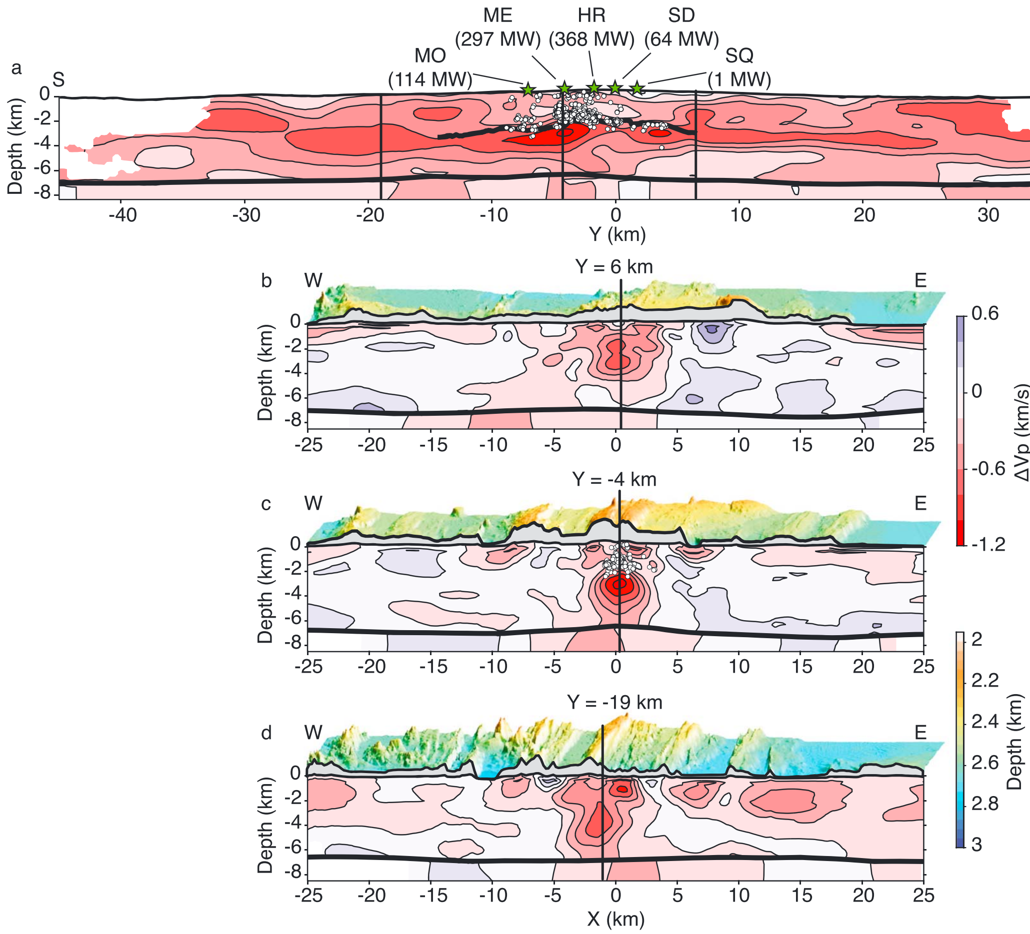

Figure 5. Vertical slices through the preferred velocity model at locations indicated in Figure 4h. (a) Vertical section showing average velocity perturbations within 400 m of the Endeavour ridge axis. The axial magma lens reflector (black line) and vent fields (green stars) are shown. Vertical black lines show the location of the cross sections shown in (b)–(d). (b–d) Vertical sections crossing the ridge axis at (b) $Y = 6$ km where the mantle magmatic system is offset relative to the ridge axis, (c) $Y = -4$ km where the mantle magmatic system is aligned with the ridge axis, and (d) $Y = -19$ km where the magmatic system is slightly offset with respect to the ridge axis. Perspective views of the overlying bathymetry are provided and vertically exaggerated by approximately 35 times. Sections show the Moho (bold black line), hypocenters for earthquakes recorded between 2003 and 2004 (Wilcock et al., 2009; white circles), and are masked where the derivative weight sum is less than 10 (see supporting information). Vertical black lines in (b)–(d) show the location of the ridge axis. Velocity perturbations are relative to the off-axis one-dimensional velocity model shown in Figure 3b (orange line).

that where the MLVZ is axis centered, the crustal low-velocity zone is more pronounced, as is ridge topography (Figure 4).

5.2. Crustal Velocity Structure

Average velocity-depth profiles (Figure 3) show significant variability in crustal structure. Off-axis regions near the segment center possess the highest average crustal velocities in the study area, increasing from 6.6 km/s at a depth of 2 km to 7.2 km/s at 6.5- to 7-km depth (blue lines, Figure 3b). These regions correlate with a broad axis-centered plateau characterized by thickened crust (Carbotte et al., 2008; Soule et al., 2016). Average, off-axis lower crustal velocities are up to 0.2 km/s slower than the ridge flanks (orange line, Figure 3b). Upper crustal (<3 km depth) velocities beneath the West Valley, Middle Valley, and North Symmetric propagating tips are slower than the model average with Middle Valley the slowest of the three (Figure 3c); low velocities in the upper-to-middle crust beneath Middle Valley have previously been attributed to thick, low-velocity sediment and an associated insulation effect that increases the temperature of the subsurface and depresses velocities (Weekly et al., 2014). Lower crustal velocities beneath these regions, however, are uniformly faster than the model average. The lowest velocities in the study area are located directly beneath the Endeavour segment (Figure 3d), with the segment center exhibiting velocities of

~6.4 km/s at 4-km depth. This slow region is capped by higher middle to upper crustal velocities that are similar to the model average, a trend not observed elsewhere on the segment. Compared to the crustal isotropic model of Soule et al. (2016), our lower crustal velocities in the off-axis regions (Figure 3b) are up to 0.3 km/s higher owing to the inclusion of anisotropy, whereas velocities beneath the rise axis (solid red line, Figure 3d) are up to 0.3 km/s lower due to the inclusion of rise-crossing *PmP* that constrain this portion of the crust. Consequently, our estimate of crustal thickness is greater than that of Soule et al. (2016), with the Middle Valley region representing the largest (~0.3 km) increase.

The segment-scale velocity structure reveals a continuous midcrustal LVV that tightly conforms to, and spans the entire length of, the ridge axis (Figure 4). The width of the LVV is approximately 5 km and relatively constant along axis. Conversely, the velocity reduction of the midcrustal anomaly varies along axis and is greatest ($\Delta Vp = -1.2$ km/s) beneath the segment center (47°55′N to 47°58′N), correlating with the location of the hydrothermal vent fields, AML reflector (Carbotte et al., 2008; Van Ark et al., 2007), and seismicity associated with magma injection (Wilcock et al., 2009; Figure 5). Beneath the E-WV OSC, the midcrustal LVV becomes more dispersed and the average velocity increases (Figures 4b–4f). The lowest crustal velocities in this region, however, still conform to the Endeavour ridge axis (Figure 4). While coverage beneath the Cobb OSC is limited, there appears to be a similar trend, though the lowest velocities deviate from the ridge axis.

The along-axis continuity of the LVV diminishes with depth, such that the LVV within the lower crust is bifurcated. From approximately 5.2-km depth to the base of the crust (average depth of 6.8 km), the LVV has higher velocities between 48°02′N and 48°05′N (Figure 5; $Y = 1$ to 15 km in Figure 5a). Interestingly, this higher-velocity region within the lower crustal LVV coincides with a 10 km westward offset of the MLVZ with respect to the ridge axis (Figure 5b). The southern lower crustal LVV largely tracks the ridge axis to the Cobb OSC and is continuous from the mantle to upper crust (Figures 5c and 5d). Conversely, the northern lower crustal LVV, which extends from 48°08′N to 48°13′N, is offset 2 km to the east of the ridge axis and coincides with the location of the inferred diking event that initiated the 2005 seismic swarm (Figure 4; Hooft et al., 2010). Resolution tests indicate the geometry of features on the order of $6 \times 6 \times 2$ km^3 is resolvable in this region of the lower crust (Figure S2), though the magnitude is underrecovered (see Text S1). We note that the 2002 multichannel seismic (MCS) survey did not detect an AML beneath this section of the ridge (Carbotte et al., 2008, 2012; Van Ark et al., 2007), which may be due to the eastward offset of the crustal LVV relative to the track of the MCS line.

5.3. Crustal Thickness Variations

Propagating limbs of the OSCs coincide with the thinnest crust within the study area (Figure 4h). The Northern Symmetric, West Valley, and Middle Valley limbs have an average crustal thickness of ~6.6 km, 0.2 km thinner than the model average, with Middle Valley limb underlain by the thinnest crust (6.4 km; Figures 3c and 4h). The thinned crust beneath North Symmetric and West Valley extend north and south of the limb tips, respectively, forming a north-south swath that projects onto the ridge axis at approximately 47°57′N, coinciding with the northern extent of the axis-centered MLVZ minima (Figure 4g). Similarly, thinned crust beneath the Middle Valley limb extends farther south than the limb tip.

Significant along-axis variability in crustal thickness epitomizes the Endeavour segment. The thinnest crust (~6.7 km) is located beneath the central portion of the segment and is 0.2 and 0.4 km thinner than at the southern and northern ends of the segment, respectively (Figure 4h). Crustal thickness beneath the southern portion of the segment is similarly variable, though it is thinner than the northern section of the segment, which displays the thickest crust beneath the ridge axis (~7.2 km). The thickened crust beneath the northern section of the Endeavour ridge extends toward the segment center to approximately 48°00′N, roughly correlating with the 10 km westward cross-axis offset of the MLVZ and associated gap in the lower crustal magmatic system (Figure 4). Within this section of the segment, the crust rapidly thickens with distance from the ridge, with a more pronounced gradient to the east of the ridge axis. This thickening gives way to the thickest crust in the study area located ~15 km off-axis.

Thickened crust is observed beneath the flanks of the segment center, coincident with the axis-centered bathymetric plateau (Figure 4h). The width and depth of the thickened crust is asymmetric about the axis, reaching a maximum thickness of 7.6 km beneath the JdF plate, compared to a maximum of 7.4 km beneath the Pacific plate. Beneath the Pacific plate, the region of thickened crust is 3 km wider than that beneath the JdF plate, coinciding with a similar asymmetry in the Brunhes/Matuyama magnetic anomaly thought to be related to the recent eastward jump of the ridge ~0.1 Ma (Carbotte et al., 2008). The region of thickened crust (i.e., crustal thickness > 7.1 km) beneath the Pacific plate is also more confined, extending from approximately 10 to 23 km off-axis, compared to the 0 to 20 km off-axis extent of thickened crust beneath the JdF plate (Figure 4h). Moreover, the thickened crust beneath the Pacific plate is located farther north, centered southwest of West Valley segment. This observed asymmetry in crustal thickness is roughly coincident with the increasing westward offset of the MLVZ relative to the ridge axis to the north (Figure 4). Specifically, the MLVZ underlies the thinner crust separating the Pacific Plate crustal thickness anomaly and the ridge axis (48°01′N, −129°08′W).

We note the discrepancy between our estimate of off-axis crustal thickness with those from other studies, including estimates from MCS data (Carbotte et al., 2008; Marjanović et al., 2011) and a previous study using the ETOMO refraction data set (Soule et al., 2016). Compared to the MCS results, our maximum estimate of crustal thickness is ~1 km thicker; we attribute this disparity to enhanced velocity control in the present study relative to that of Marjanović et al. (2011), which utilized a constant crustal velocity to estimate crustal thickness. While our estimate of off-axis crustal thickness is more comparable to that of Soule et al. (2016), it is up to 0.1 to 0.3 km thicker. We attribute this increased crustal thickness to the influence of crustal anisotropy on *PmP* traveltimes. The crustal HTI medium, defined by fast directions oriented in the ridge-parallel and vertical directions, effectively decreases *PmP* traveltimes relative to the isotropic case, as *PmP* waves predominately propagate in the vertical dimension. Consequently, accounting for upper crustal crack-induced anisotropy yields systematically larger crustal thickness estimates. Thus, incorporation of anisotropy in our analysis could account for the increased crustal thickness in our study compared to the isotropic results of Soule et al. (2016).

6. Discussion

We constrain the three-dimensional segment-scale structure of the topmost mantle and crust beneath an active oceanic spreading center. Our results allow us to estimate the physical properties of the axial region. The observed LVV extending from the mantle to the midcrust cannot be entirely explained by variations in subsolidus temperature and requires the presence of partial melt. We infer that this LVV reflects the geometry of the axial magmatic system. Thus, our results provide novel insights into the magma plumbing system beneath an entire ridge segment, the influence of skewed delivery of mantle melt on along-axis variability in magmatic and hydrothermal processes, and the relationship between crustal thickness, magma supply, and the tectonic evolution of a ridge segment. We discuss each of these topics in turn.

6.1. Estimates of Physical Properties

To estimate the temperature and melt fraction variations consistent with the tomographic results, we apply the method of Dunn et al. (2000). This process involves two steps: (i) estimating the velocity reduction that can be attributed to a thermal anomaly and (ii) interpreting the remaining velocity reduction in terms of melt fraction. The former attempts to explain the sensitivity of seismic velocity to the anharmonic and anelastic effects of temperature (Karato, 1993):

$$\frac{\partial \ln Vp}{\partial T} = \left.\frac{\partial \ln Vp}{\partial T}\right|_{\text{anharmonic}} - F(\alpha)\frac{Q(f,T)^{-1}}{\pi}\frac{H^*}{RT} \tag{2}$$

where Vp is the compressional wave velocity, T is temperature, $F(\alpha)$ has a value near 1, α is the frequency dependence of Q, Q is the quality factor, f is frequency, H^* is an activation enthalpy, and R is the universal gas constant. The first term on the right-hand side of equation (2) represents the temperature derivative due to anharmonic effects, which do not involve seismic energy loss and are independent of frequency. The second term represents the temperature derivative due to anelastic effects, which are associated with intrinsic attenuation and are frequency dependent. The anelastic term is spatially variable owing to the spatial dependence of Q, H^*, and T. In regions where Q is large (>500), the anelastic term is negligible. Conversely, where Q is small (<100), the anelastic term is significant. We define the reference Q structure to be the average off-axis Q structure for the EPR (Wilcock et al., 1995). The axial Q structure is subsequently modified based upon the anharmonic thermal structure, discussed below. We define two values of H^* for the

10.1029/2018GC007978

Table 1
Scaling Relations and Constants

Relation	Value	Reference
H^*_{crust}	276 kJ/mol	Caristan (1982)
H^*_{mantle}	500 kJ/mol	Jackson et al. (1992)
$\left(\frac{\partial \ln Vp}{\partial T}\right)_{\text{crust, anharmonic}}$	-8.1×10^{-5} K^{-1}	Christensen and Salisbury (1979)
$\left(\frac{\partial \ln Vp}{\partial T}\right)_{\text{mantle, anharmonic}}$	-6.2×10^{-5} K^{-1}	Isaak (1992)
$\left(\frac{\partial \ln Vp}{\partial \phi}\right)_{\text{gabbro, melt in tubules}}$	-0.76	Canales et al. (2014) and Mavko (1980)
$\left(\frac{\partial \ln Vp}{\partial \phi}\right)_{\text{peridotite, melt in tubules}}$	-0.86	Canales et al. (2014) and Mavko (1980)
$\left(\frac{\partial \ln Vp}{\partial \phi}\right)_{\text{melt in films}}$	-3	Dunn et al. (2000) and Schmeling (1985)

crust and mantle and set those values within the model to the appropriate value in Table 1. There is significant uncertainty in the values that control the anelastic term. We therefore assume the maximum possible contribution of the anelastic term by setting $F(\alpha) = 1$ and substitute the appropriate values in Table 1 into equation (2).

We derive a thermal model for the preferred velocity structure that considers both anharmonic and anelastic effects (Figure 6a). To estimate the thermal structure, the velocity perturbation model is used to calculate temperature perturbations relative to a reference, 10 km off-axis, one-dimensional temperature profile characteristic of oceanic crust (Dunn et al., 2000; Figure S6). Since subaxial temperatures are not expected to exceed 1150 °C (Sinton & Detrick, 1992), we prevent perturbations that exceed this temperature so as to explain as much of the velocity reduction as possible in terms of a thermal anomaly; if we did not do so, temperatures in excess of 3000 °C would be required to explain the observed velocity reduction in terms of anelastic temperature alone. We first calculate an anharmonic thermal model using only the first term of equation (2), which serves as the initial thermal structure for subsequent calculation of the anelastic thermal model and is used to modify the Q structure (Figure S7a). Specifically, we set $Q = 100$, the average Q value of the lower crust in the axial region of the EPR (Wilcock et al., 1995), where the anharmonic temperature estimate is above the temperature cutoff of 1150 °C. To construct the anelastic thermal model, we used the appropriate values in Table 1 and the anharmonic T and Q models. Because the temperature derivative is itself temperature dependent, we ran several iterations of equation (2) to derive the anelastic temperature. Beginning with the anharmonic thermal structure, we calculated a new temperature derivative and thermal structure for each iteration. The resultant thermal structure was then used as the new temperature model for the subsequent iteration. Iteration was ended once the maximum difference between the current and previous iteration was everywhere less than 10 °C.

As at the EPR, the predicted cross-axis thermal structure beneath the Endeavour segment is steep sided (Figures 6a and S7a; Dunn et al., 2000). Moreover, our thermal model shows that anomalously high crustal temperatures are restricted to a narrow region within ~5 km of the ridge axis, similar to results from the EPR (Dunn et al., 2000). Off-axis isotherms, however, are not completely horizontal as at the EPR and instead have depressions that coincide with the edges of the MLVZ ($X = -6$ and 8 km, Figure 6a), a feature that is asymmetric about the rise axis. To the west of the ridge axis, the isotherms are largely horizontal, with the exception of a small depressed zone located approximately 5 to 8 km off-axis. A more pronounced zone of depressed isotherms is located 6 to 10 km to the east of the ridge axis. Both of these zones coincide with the location of prominent elongate abyssal hills on the seafloor, inferred to be the former ridge axis (Carbotte et al., 2008). These depressions could therefore be indicative of enhanced hydrothermal circulation further off-axis or alternatively, the result of patterns of melt delivery, which we discuss in section 6.2.

Temperature alone cannot fully explain the magnitude of the velocity anomaly, and melt must be present to explain a significant portion of the LVV. The thermal contribution to the observed velocity reduction is 46% and 57% for the anharmonic and anharmonic plus anelastic case, respectively. An estimate of the melt

10.1029/2018GC007978

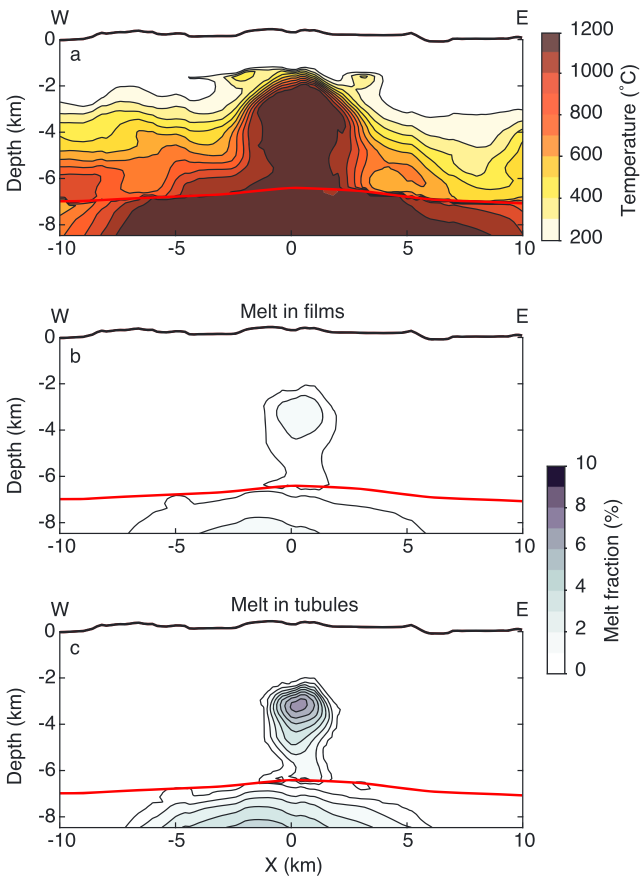

Figure 6. Temperature and melt fraction models computed from the cross-axis section in Figure 5c. Temperature and melt fraction are contoured at 100 °C and 1%, respectively. (a) Temperature model assuming anharmonic and anelastic effects. (b) Melt fractions calculated assuming anharmonic plus anelastic effects for which melt resides in thin films. (c) As for (b), except for melt residing in tubules. Large velocity reductions above 2-km depth (e.g., Figure 5) are attributed to porosity variations and are therefore removed from the temperature and melt fraction calculations.

fraction within a LVV depends upon the melt distribution within the rock matrix (Mavko, 1980; Schmeling, 1985). Here, we estimate melt content using the residual velocity anomalies (i.e., with thermal effects removed) for two possible cases of melt distribution: films and tubules. We use the *Vp* dependence on melt fraction for relaxed films reported by Dunn et al. (2000), using the formulation of Schmeling (1985; Table 1). For tubules, we implement the *Vp* dependence on melt fraction for crustal and mantle rocks derived by Canales et al. (2014) using the formulation of Mavko (1980; Table 1). These values provide lower and upper bounds for the melt fraction in regions where temperature alone cannot account for observed velocity anomalies. For the anharmonic case, we get maximum melt percentage of 3% and 12% for melt residing in films and tubules, respectively (Figures S7b and S7c). We get a maximum melt percentage of 1% and 7% for films and tubules in the case where anelasticity is important (Figures 6b and 6c). On the basis of these results, we infer the LVV that persists from the topmost mantle to mid-crust to be the magmatic system.

Computing temperatures and melt fractions from velocity is complicated by large sources of uncertainty. Principle among these are the (i) reference thermal structure used to compute the temperatures within the LVV, (ii) *Q* structure and frequency effects, (iii) geometry of the interstitial melt distribution, and (iv) underresolution of velocity anomalies. Consequently, a suite of feasible choices of parameters exist that give rise to substantially different estimates of these physical parameters. For instance, choosing a colder reference thermal structure (Figure S6) produces a thermal model that requires less melt and a narrower melt-containing region at midcrustal depths (Figure S8). Conversely, our study underestimates the amplitude of velocity anomalies by approximately 50%, though it does provide a good indication of spatial variations in velocity and hence, relative melt content (Figure S2). Our analysis therefore provides a first-order estimate of the thermal structure and melt distribution beneath the Endeavour segment.

6.2. Melt Distribution Within the Mantle and Crustal Magmatic Systems

Significant variations in melt volume are observed beneath the nonoverlapping portion of the Endeavour segment (Figure 7). Mantle melt volume in the nonoverlapping domain displays three prominent maxima (labeled I, II, and III in Figure 7), with the two southern maxima roughly correlating with elevated crustal melt volumes and the along-axis extent of the AML (47°52′N to 48°02′N) imaged beneath the Endeavour (Carbotte et al., 2012; Van Ark et al., 2007). Crustal melt volumes within this section of ridge diminish northward, coincident with the increasing westward offset of the melt-containing region in the mantle (Figure 7). The minimum crustal melt volumes observed along the entirety of the Endeavour segment are associated with the maximum (10 km) offset of the mantle magmatic system with respect to the ridge axis (48°02′N to 48°05′N; Figure 7d); within this portion of the segment, the lower crust has little to no melt present (Figure 7b). Interestingly, the southern (48°02′N) extent of this low-melt zone is coincident with a deviation from axial linearity (Karsten et al., 1990), or deval, and the northernmost extent of the AML. Similarly, the northern (48°05′N) extent of this zone coincides with an abrupt discontinuity in tectonic fabric (Karsten et al., 1986). Another deval, located at 47°55′N (Karsten et al., 1990), correlates with the southern extent of the prominent, midcrustal melt anomaly (Figure 7a). These results suggest a significant link between the skew of the mantle and crustal magmatic systems, the efficiency of melt transport from the mantle to the crust, and tectonic structure of the ridge.

Coincidence between along-axis variations in melt content beneath the Endeavour and seafloor features are similar to results from the EPR, suggesting that variations in mantle melt delivery induce tectonic and

 10.1029/2018GC007978

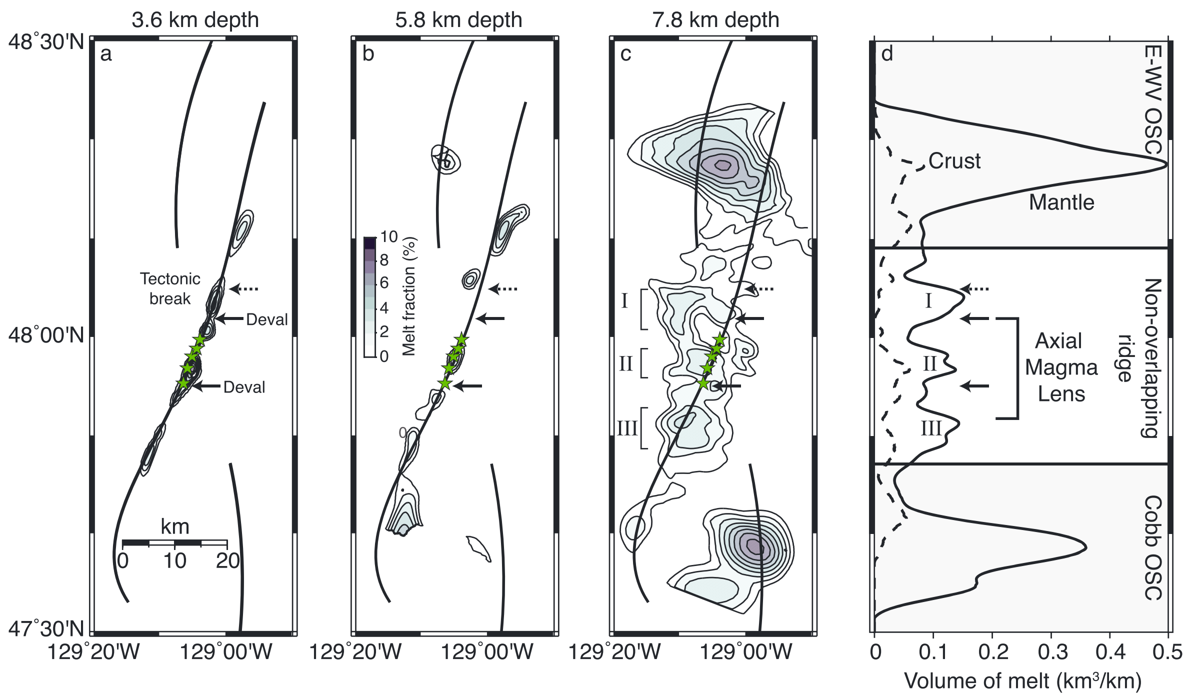

Figure 7. Along-axis variations in melt content. (a–c) Map view sections are taken at (a) 3.6-km depth, (b) 5.8-km depth, and (c) 7.8-km depth, corresponding to the midcrustal, lower crustal, and mantle portions of the magmatic system, respectively. Sections are for the model in Figure 6c. (d) Along-axis melt volume per kilometer of crust (dashed black line) and mantle (solid black line). The along-axis extent of the axial magma lens reflector is also shown (Van Ark et al., 2007). Solid black arrows denote devals (Karsten et al., 1990), the dashed arrow indicates an abrupt discontinuity in the tectonic fabric (Karsten et al., 1986), and green stars show vent field locations. Calculated melt fractions assume anharmonic and anelastic effects with melt residing in tubules. Regions with a derivative weight sum <10 do not contribute to the estimation, nor do regions in the model space with >4% anisotropy. E-WV = Endeavour-West Valley; OSC = overlapping spreading center.

magmatic segmentation. At the EPR, away from tectonic discontinuities such as transform faults or OSCs, the ridge is segmented at the scale of ~20–25 km, referred to as third-order or volcanic segments (Langmuir et al., 1986; Macdonald et al., 1988; Toomey et al., 2007; White et al., 2002). The centers of those third-order segments are associated with higher eruption effusion rates (White et al., 2002) and their boundaries coincide with discontinuities in the AML (Carbotte et al., 2013; Marjanović et al., 2014), giving rise to the notion that each third-order segment is fed by a distinct crustal magmatic system consisting of a central volcano and associated dikes and fissures (White et al., 2000, 2002). Centers of mantle melt delivery beneath the EPR are similarly spaced at intervals of ~25 km, suggesting the third-order segmentation and associated magmatic segmentation is governed by variations in mantle melt delivery (Toomey et al., 2007). While third-order segmentation has hitherto been poorly defined at the Endeavour segment, the coincidence between the imaged LVVs with seafloor features suggest that it is segmented at a scale of ~15 km (Figure 7). Similar to the EPR, third-order segmentation of the Endeavour appears to be related to mantle melt delivery.

The northernmost crustal melt anomaly beneath the Endeavour segment, extending from 48°08′N to 48°13′N, is associated with a section of the ridge that overlaps the West Valley segment (Figure 7b). Here, the crustal melt anomaly is centered approximately 2 km to the east of the ridge axis and is vertically continuous from lower to midcrustal depths. Of note is that this crustal anomaly does not directly overlie a mantle melt anomaly, though it is centered approximately 10 km south of the broad region of enhanced melt beneath the E-WV OSC (Figures 7b and 7c). Resolution within this portion of the model space suggests that the northern extent of the crustal melt anomaly is not well recovered within the lower crust (Figures S2b and S2c). We therefore postulate that this feature is associated with the E-WV mantle melt region.

The greatest volumes of mantle melt are located beneath the two second-order discontinuities bounding the Endeavour segment. By volume, the Cobb and E-WV OSCs contain up to 70% and 60% more mantle melt than the nonoverlapping region of the Endeavour segment, respectively (Figure 7d). This is consistent with previous results that suggest OSCs are regions of enhanced mantle melt retention (VanderBeek et al., 2016). Enhanced crustal melt retention beneath OSCs has also been inferred from seismic imaging of crustal structure along the EPR (Bazin et al., 2003) and Lau Spreading Center (Dunn et al., 2013; Turner et al., 1999), which identify anomalously broad crustal magmatic systems spanning OSCs. Moreover, MCS imaging experiments from both the EPR (Kent et al., 2000) and Lau Basin (Collier & Sinha, 1992) reveal that widespread crustal melt lenses are characteristic of OSCs. Our crustal resolution, however, is limited beneath the OSCs such that we are unable to accurately estimate the volume of crustal melt in these regions (Figure S2). Thus, while our results agree with previous studies that infer second-order discontinuities are sites of enhanced mantle melt retention, they cannot confirm whether they are also sites of broad, enhanced crustal melt retention owing to limited resolution.

6.3. Skew Between the Mantle and Crustal Magmatic Systems

We infer that the observed skew between the mantle and crustal magmatic systems is a direct result of differences in mechanisms of heat transfer at crustal and mantle depths. At crustal depths we infer that hydrothermal processes extend throughout the crust and efficiently transport heat, giving rise to a steep-sided, relatively narrow magmatic system confined to the axis of tectonic rifting (Figures 6a). Asymmetry in the thermal structure may indicate uneven rates of hydrothermal cooling, whereas depressed isotherms up to 10 km off-axis may further suggest a significant component of off-axis circulation, though this remains speculative as we are unable to discern between compositional changes and thermal variations off-axis, which could also give rise to the observed velocity variations (Figure 5c). Pervasive crustal-scale hydrothermal circulation has previously been inferred from in situ analysis of the Oman ophiolite (e.g., Gregory & Taylor, 1981), the thermal structure of young oceanic crust (Dunn et al., 2000), and hydrothermal circulation models (Hasenclever et al., 2014). While tectonic extension along the plate boundary defines the location of magma intrusion, it is pervasive crustal-scale hydrothermal circulation that controls the depth of the melt lens (Chen & Morgan, 1996), determines the thermal structure of young oceanic crust (Hasenclever et al., 2014), and controls the cross-axis width of the crustal magmatic system (Dunn et al., 2000). On the basis of our results and those from the EPR, we conclude that when a long-lived, crustal melt lens is present at fast- or intermediate-spreading rates, the overall shape of the magmatic system is governed by a thermal structure that results from the interplay among tectonic extension, magma injection, and crustal-scale hydrothermal circulation.

Our results, together with those of VanderBeek et al. (2016), strongly suggest that at mantle depths advective heat removal is greatly diminished and conduction is the primary means of heat transport. This inference is consistent with the abrupt increase in the width of magmatic system from 5- to 20-km width (Figure 6a). VanderBeek et al. (2016) suggest that shallow mantle melt distribution beneath mid-ocean ridges is controlled by three-dimensional variations in the thickness of near-ridge lithosphere. In this case, mantle melt accumulations would increase wherever the lithosphere is youngest and thinnest, owing to the topography of the thermal boundary layer (Sparks & Parmentier, 1991). Indeed, the north-south trend of the mantle magmatic system is subparallel to the thinnest crust, and by inference, the hottest and thinnest lithosphere (Figures 4g and 4h). We therefore conclude that the width and trend of the mantle magmatic system is determined by the regional-scale, mantle thermal structure of the northern JdFR, which is in turn controlled by the overlying rift geometry. Conductive heat loss is proportional to the thermal gradient and will be greater where isotherms are shaped by hydrothermal circulation at crustal depths. Thus, the mantle magmatic system is narrow beneath the segment center where hydrothermal circulation is vigorous and broad beneath the OSCs, where heat is less efficiently mined via advection.

We observe that crustal magmatic and hydrothermal activity correlate with along-axis variability in skew and are enhanced in regions where skew is minimal. Within the central portion of the Endeavour segment, mantle melt delivery is axis centered, coincident with the presence of an AML, enhanced crustal melt volume, and extensive hydrothermal activity consisting of >800 individual chimneys within a 15-km along-axis span (Kelley et al., 2012, and references therein; Figures 4 and 7). This region was also a site of intense seismicity associated with magma lens replenishment (Wilcock et al., 2009). Ridge topography in the segment center, consisting of an axial high and prominent abyssal hills, indicate enhanced magmatic activity within the recent geologic past (Clague et al., 2014). In contrast, where mantle melt delivery is predominantly off-axis (to the north and south of the segment center), an AML is absent, crustal melt volumes

10.1029/2018GC007978

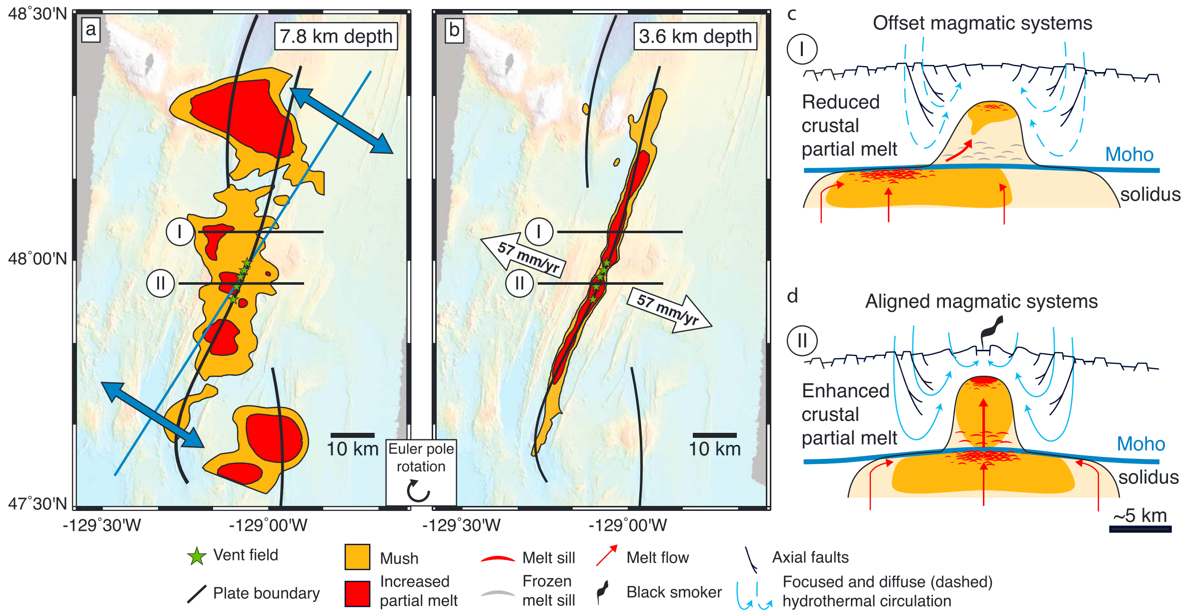

Figure 8. Conceptual diagram illustrating how skew within the magmatic system influences magmatic and hydrothermal activity. (a) Map view section showing the north–south structure of the mantle magmatic system. The axis (blue line) and direction (blue arrows) of mantle divergence are overlain. Yellow and red contours in (a) demarcate regions containing low (~0%) and higher (3%) melt fractions, respectively (Figure 7c). (b) Map view section showing the ridge-tracking structure of the crustal magmatic system. Yellow and red contours show region with velocity reductions of −0.6 and −0.8 km/s, respectively (Figure 4c). The white arrows show spreading direction and full-spreading rate (Gripp & Gordon, 2002). Recent rotation in the Euler pole of the Juan de Fuca-Pacific plate system is indicated (Wilson, 1988). The lines labeled as I and II in (a) and (b) correspond to the cross sections shown in (c) and (d), respectively. (c) If the mantle and crustal magmatic systems are offset, melt transport from the mantle to the crust is inefficient, resulting in less frequent crustal replenishment. Consequently, low degrees of partial melt are present within the crust and hydrothermal clogging reduces crustal permeability, resulting in diffuse hydrothermal activity. (d) If the mantle and crustal magmatic systems are aligned, melt transport from the mantle to the crust is focused and efficient, such that enhanced partial melt is present at crustal depths. The frequent crustal replenishment induces seismogenic cracking that locally enhances crustal permeability (Wilcock et al., 2009), facilitating vigorous hydrothermal circulation. Panels (c) and (d) are modified from Toomey et al. (2007).

decrease, and hydrothermal activity is diminished (Figure 7). The lowest crustal melt volumes present along the Endeavour segment are found where the MLVZ is farthest from the rise axis (48°02′N to 48°05′N, Figure 7d). These relations suggest axis-centered delivery of mantle melt exerts a primary control on magmatic and hydrothermal activity at mid-ocean ridges.

Our results, combined with those of previous studies, provide a conceptual model of how skew between mantle and crustal magmatic reservoirs governs along-axis, segment-scale variations in volcanic, magmatic, and hydrothermal activity at mid-ocean ridges (Figure 8). Beneath nonoverlapping ridge segments, mantle-derived melts are focused and efficiently transported from the mantle to the crust where the magma reservoirs are vertically aligned (Figures 8a, 8b, and 8d), resulting in a continuous magmatic system that extends from the topmost mantle to the midcrust. We suggest that this efficient melt transport results in more frequent crustal magma injection and high degrees of partial melt at crustal depths. The frequency of magma injection is thought to determine the permeability structure of the overlying crust (Wilcock et al., 2009) via seismogenic cracking of the thermal boundary layer separating the magmatic and hydrothermal systems, thereby maintaining permeable pathways and facilitating efficient hydrothermal circulation (Arnoux et al., 2017). Thus, where the cross-axis offset between the mantle and crustal magmatic systems is minimal, crustal magmatic and hydrothermal activity are enhanced. This is supported by the correlation between the vertically aligned magmatic systems in the segment center with seismicity associated with magma injection (Wilcock et al., 2009) and the presence of vigorous, high-temperature hydrothermal venting (Figure 5). Alternatively, where the locus of the mantle melt delivery is predominantly off-axis and the mantle and crustal magmatic systems are not vertically aligned, such as between 48°02′N and 48°05′N (Figure 7b), vertical melt transport is less efficient (Figure 8c). Owing to this inefficient melt delivery, magma injection is less frequent, resulting in the closure of permeable pathways and diminished hydrothermal venting (Figure 8c). It may be that in such sections of ridge, along-axis transport of melt within the midcrustal reservoir plays a more prominent role in upper crustal accretion. The tectonic fabric may also be influenced in cases of off-axis delivery of mantle melt, such as the abrupt discontinuity observed at 48°05′N (Figure 7; Karsten et al., 1986).

Our model predicts that magma entering the crustal system where the two magmatic systems are vertically aligned will have undergone rapid ascent and relatively less differentiation. Extreme variability in lava enrichment is observed in the center of the Endeavour segment, coincident with axis-centered mantle melt delivery. Such a breadth of enrichment suggests reduced magma mixing and more rapid magma ascent so as to preserve distinct mantle signatures (Karsten et al., 1990). Lower crustal velocities near the segment center are higher than elsewhere along the ridge (Figures 4 and 5c) and further support that it has undergone comparatively less differentiation (Soule et al., 2016). A progressive decrease in the level of lava enrichment northward from the segment center is consistent with mixing of magmas or sources (Karsten et al., 1990). Interestingly, this trend coincides with increasing off-axis mantle melt delivery and a decrease in lower crustal velocities flanking the magmatic system (e.g., Figure 5d), potentially indicating higher degrees of differentiation (Toomey & Hooft, 2008). In our model, the vertical alignment of the mantle and crustal magmatic systems controls not only the frequency of crustal magma injection but also magma residence time and differentiation.

6.4. Segment-Scale Magma Transport

Along-axis crustal thickness variations do not require centralized, focused magma supply. The segmentation of mid-ocean ridges has often been attributed to magma supply (Francheteau & Ballard, 1983; Macdonald et al., 1988, 1991; Schouten et al., 1985; Whitehead et al., 1984), which predicts that the morphology of the ridge axis reflects the local supply of magma, with enhanced magma supply and hence, the thickest crust, at the center of ridge segments (Macdonald et al., 1988, 1991; Schouten et al., 1985). Conversely, segment ends are predicted to be magma starved (i.e., reduced magma supply), resulting in thinner crust and greater axial depth. We observe the opposite spatial relationship to these predictions at the Endeavour segment. Within the central portion of the segment, where the mantle and crustal magmatic systems are aligned and vigorous hydrothermal and magmatic activity persist, crustal thickness is 0.2–0.4 km thinner than the segment ends (Figure 4h). A similar association between axis-centered mantle melt supply and thin crust has been inferred at the EPR from 9°40′N to 9°50′N (Barth & Mutter, 1996; Canales et al., 2003; Toomey et al., 2007) and analysis of flow structures in lower crustal and mantle rocks in the Oman ophiolite show that localized upwelling zones underlie the thinnest crust and crustal thickness gradually increases away from such zones (Nicolas et al., 1996). Furthermore, observations of diking events on the Endeavour provide evidence for along-axis melt transport not only from the segment center toward the segment end (Bohnenstiehl et al., 2004) but also from the segment end to the segment center (Hooft et al., 2010). Our results, in conjunction with these observations, are inconsistent with enhanced melt supply beneath the segment center that is redistributed toward segment ends. In agreement with previous studies (Barth & Mutter, 1996; Canales et al., 2003; Toomey & Hooft, 2008), we infer that the relationship between magma supply, crustal thickness, and axial depth is not as straightforward as commonly assumed.

Correlation between the diking events and intrasegment velocity structure suggests that vertical melt transport is significant and likely controls the observed along-axis crustal thickness variations (Figure 4). During the 1999 diking event, seismic activity initiated near the central portion of the segment, roughly coincident with vertically aligned magmatic system and the location of a shallow AML (Carbotte et al., 2012; Van Ark et al., 2007), and subsequently migrated ~12 km to the south along the southern end of the Endeavour segment (Bohnenstiehl et al., 2004). Contrary to the 1999 diking event, the 2005 diking event was initiated in the northern end of the segment (48°10′N) and propagated ~20 km from segment end toward the segment center (Hooft et al., 2010; Weekly et al., 2013). The initiation of the 2005 event correlates with the eastward offset of the crustal LVV (Figure 4), though the connection of this crustal anomaly to the mantle is unclear. One possibility is that it is linked to the MLVZ beneath the E-WV OSC. Our resolution, however, is insufficient to confirm this. Of note is the 15-km-long zone of high velocities and low-melt content within the lower crust separating the two sites where the diking events initiated (Figures 5a and 7b), whose boundaries generally coincide with changes in seafloor fabric (Figure 7). On the basis of these observations, we suggest that melt transport within the lower crust is predominantly vertical and fundamental to the genesis of oceanic crust at the Endeavour segment.

10.1029/2018GC007978

What gives rise to the highly heterogeneous nature of crustal thickness off-axis is equivocal. For instance, asymmetric, thickened crust beneath the broad axis-centered plateau may be consistent with either enhanced magmatism in the past relative to the rest of the segment (Carbotte et al., 2008) or the southward propagation of the Endeavour segment 0.71 Ma and associated tapping of mantle melt pooled beneath the Cobb OSC (Figure 4h; Soule et al., 2016; VanderBeek et al., 2016). Similarly, thinned crust associated with the propagating limbs in the region may be consistent with tectonically driven ridge propagation or indicative of a reduction in magma supply, such as that inferred for parts of the Mid-Atlantic Ridge (Kleinrock et al., 1997). Thus, the significant heterogeneity in off-axis crustal thickness is an enigma stemming from the complex tectonic reorganization of the Endeavour segment and, consequently, difficult to explain with simple models of mid-ocean ridge segmentation.

7. Conclusions

1. We image a distinct difference between the trend of the crustal and mantle LVVs. The crustal LVV closely tracks the ridge axis, whereas the mantle LVV trends north-south, subparallel to the regional trend of the northern JdF plate boundary, connecting the two OSCs bounding the segment.
2. We estimate, to first order, the thermal structure and melt distribution beneath the Endeavour segment. The steep-sided, narrow structure of the crustal thermal anomaly indicates that it is shaped by pervasive crustal-scale hydrothermal circulation. An abrupt increase in width of the thermal anomaly across the Moho suggests that advective heat removal is less efficient than in the crust. We conclude that the width and trend of the mantle magmatic system is instead determined by the regional-scale, mantle thermal structure of the northern JdFR.
3. Segment-scale skew, or lateral offset, between the mantle and crustal magmatic systems induces segment-scale variations in magmatic and hydrothermal activity at mid-ocean ridges. Previous studies have proposed a model in which sites of axis-centered melt delivery exhibit frequent crustal magma replenishment, vigorous hydrothermal activity, and other ridge crest processes (Toomey et al., 2007; VanderBeek et al., 2016). Conversely, infrequent crustal magma replenishment and decreased hydrothermal activity typify sites of off-axis melt delivery. Ours is the first study to image the segment-scale structure of the magmatic system from the topmost mantle to upper crust and show such a link exists. The crustal magmatic system is most prominent where mantle melt delivery is axis centered, coincident with vigorous hydrothermal venting, the along-axis extent of the imaged AML (Carbotte et al., 2012; Van Ark et al., 2007), and recent magma chamber inflation (Wilcock et al., 2009). Conversely, where mantle melt delivery is off-axis, estimated crustal melt content is greatly reduced, hydrothermal activity is weak or absent, and an AML is nonexistent.
4. Correlation between along-axis variations in estimated melt content and transitions in seafloor fabric suggest tectonic and magmatic segmentation on the order of ~15 km.
5. Along-axis crustal thickness variations do not require centralized magma supply. The magma supply model predicts enhanced magma supply and thickened crust beneath segment centers, whereas segment ends are magma starved with thinner crust (Macdonald et al., 1988, 1991; Schouten et al., 1985). We observe the opposite spatial relationship to these predictions, in which the segment ends display thicker (0.2–0.4 km) crust relative to the segment center. Moreover, dike propagation events along the Endeavour (Bohnenstiehl et al., 2004; Hooft et al., 2010; Weekly et al., 2013) have propagated from segment center to end, as well as segment end to center, indicating along-axis melt transport initiates from both the segment center and ends.

Acknowledgments
We thank the officers and crew of the R/V *Marcus G. Langseth* as well as the ocean bottom seismometer teams from Scripps Institution of Oceanography and Woods Hole Oceanographic Institution for their assistance in the acquisition of the seismic data. Additional assistance was provided by on-board passive acoustic technicians and marine mammal observers to ensure that data collection was accomplished in compliance with guidelines set forth by marine environmental assessments and permits. We also thank Lindsay Worthington and an anonymous reviewer for their constructive reviews, which helped improve the manuscript. The experiment and analysis were supported by the NSF under grants numbered OCE-0454700 to the University of Washington and OCE-0454747, OCE-0651123, and OCE-1634786 to the University of Oregon. The seismic data set used in this study is available on request through the IRIS-DMC (report number 09-014; http://ds.iris.edu/ds/nodes/dmc). The ETOMO cruise report can be accessed at http://pages.uoregon.edu/drt/MGL0910_Science_Report website.

References

Arnoux, G. M., Toomey, D. R., Hooft, E. E. E., Wilcock, W. S. D., Morgan, J., Warner, M., & VanderBeek, B. P. (2017). Seismic evidence that black smoker heat flux is influenced by localized magma replenishment and associated increases in crustal permeability. *Geophysical Research Letters*, *44*, 1687–1695. https://doi.org/10.1002/2016GL071990

Barclay, A. H., & Toomey, D. R. (2003). Shear wave splitting and crustal anisotropy at the Mid-Atlantic Ridge, 35°N. *Journal of Geophysical Research*, *108*(B8), 2378. https://doi.org/10.1029/2001JB000918

Barclay, A. H., Toomey, D. R., & Solomon, S. C. (1998). Seismic structure and crustal magmatism at the Mid-Atlantic Ridge, 35°N. *Journal of Geophysical Research*, *103*, 17,827–17,844. https://doi.org/10.1029/98JB01275

Barth, G. A., & Mutter, J. C. (1996). Variability in oceanic crustal thickness and structure: Multichannel seismic reflection results from the northern East Pacific Rise. *Journal of Geophysical Research*, *101*, 17,951–17,975. https://doi.org/10.1029/96JB00814

Bazin, S., Harding, A. J., Kent, G. M., Orcutt, J. A., Singh, S. C., Tong, C. H., et al. (2003). A three-dimensional study of a crustal low velocity region beneath the 9°03′N overlapping spreading center. *Geophysical Research Letters*, *30*(2), 1039. https://doi.org/10.1029/2002GL015137

Bell, R. E., & Buck, W. R. (1992). Crustal control of ridge segmentation inferred from observations of the Reykjanes Ridge. *Nature*, *357*(6379), 583–586. https://doi.org/10.1038/357583a0

Bohnenstiehl, D. R., Dziak, R. P., Tolstoy, M., Fox, C. G., & Fowler, M. (2004). Temporal and spatial history of the 1999–2000 Endeavour Segment seismic series, Juan de Fuca Ridge. *Geochemistry, Geophysics, Geosystems*, *5*, Q09003. https://doi.org/10.1029/2004GC000735

Butterfield, D. A., McDuff, R. E., Mottl, M. J., Lilley, M. D., Lupton, J. E., & Massoth, G. J. (1994). Gradients in the composition of hydrothermal fluids from the Endeavour segment vent field: Phase separation and brine loss. *Journal of Geophysical Research*, *99*, 9561–9583. https://doi.org/10.1029/93JB03132

Byrnes, J. S., Toomey, D. R., Hooft, E. E. E., Nábělek, J., & Braunmiller, J. (2017). Mantle dynamics beneath the discrete and diffuse plate boundaries of the Juan de Fuca plate: Results from Cascadia Initiative body wave tomography. *Geochemistry, Geophysics, Geosystems*, *18*, 2906–2929. https://doi.org/10.1002/2017GC006980

Canales, J. P., Detrick, R. S., Toomey, D. R., & Wilcock, W. S. D. (2003). Segment-scale variations in the crustal structure of 150–300 kyr old fast spreading oceanic crust (East Pacific Rise, 8°15′N–10°5′N) from wide-angle seismic refraction profiles. *Geophysical Journal International*, *152*(3), 766–794. https://doi.org/10.1046/j.1365-246X.2003.01885.x

Canales, J. P., Dunn, R. A., Ito, G., Detrick, R. S., & Sallarès, V. (2014). Effect of variations in magma supply on the crustal structure of Mid-Ocean Ridges: Insights from the Western Galápagos spreading center. In N. d'Ozouville, D. Graham, K. Harpp, & E. Mittelstaedt (Eds.), *The Galapagos: A Natural Laboratory for the Earth Sciences* (pp. 363–391). Hoboken, NJ: John Wiley & Sons. https://doi.org/10.1002/9781118852538.ch17

Carbotte, S. M., Canales, J. P., Nedimović, M., Carton, H., & Mutter, J. (2012). Recent seismic studies at the East Pacific Rise 8°20′–10°10′N and Endeavour Segment: Insights into mid-ocean ridge hydrothermal and magmatic processes. *Oceanography*, *25*(1), 100–112. https://doi.org/10.5670/oceanog.2012.08

Carbotte, S. M., Detrick, R. S., Harding, A., Canales, J. P., Babcock, J., Kent, G., et al. (2006). Rift topography linked to magmatism at the intermediate spreading Juan de Fuca Ridge. *Geology*, *34*(3), 209–212. https://doi.org/10.1130/G21969.1

Carbotte, S. M., Marjanović, M., Carton, H., Mutter, J. C., Canales, J. P., Nedimović, M. R., et al. (2013). Fine-scale segmentation of the crustal magma reservoir beneath the East Pacific Rise. *Nature Geoscience*, *6*(10), 866–870. https://doi.org/10.1038/ngeo1933

Carbotte, S. M., Nedimović, M. R., Canales, J. P., Kent, G. M., Harding, A. J., & Marjanović, M. (2008). Variable crustal structure along the Juan de Fuca Ridge: Influence of on-axis hot spots and absolute plate motions. *Geochemistry, Geophysics, Geosystems*, *9*, Q08001. https://doi.org/10.1029/2007GC001922

Caristan, Y. (1982). The transition from high temperature creep to fracture in Maryland diabase. *Journal of Geophysical Research*, *87*, 6781–6790. https://doi.org/10.1029/JB087iB08p06781

Chen, J., & Morgan, J. P. (1996). The effects of spreading rate, the magma budget, and the geometry of magma emplacement on the axial heat flux at mid-ocean ridges. *Journal of Geophysical Research*, *101*, 11,475–11,482. https://doi.org/10.1029/96JB00330

Christensen, N. I., & Salisbury, M. H. (1979). Seismic anisotropy in the oceanic upper mantle: Evidence from the Bay of Islands Ophiolite Complex. *Journal of Geophysical Research*, *84*, 4601–4610. https://doi.org/10.1029/JB084iB09p04601

Clague, D. A., Dreyer, B. M., Paduan, J. B., Martin, J. F., Caress, D. W., Guilderson, T. P., & Mcgann, M. L. (2014). Eruptive and tectonic history of the Endeavour Segment, Juan de Fuca ridge, based on AUV mapping data and lava flow ages. *Geochemistry, Geophysics, Geosystems*, *15*, 3364–3391. https://doi.org/10.1002/2014GC005415

Collier, J. S., & Sinha, M. C. (1992). Seismic mapping of a magma chamber beneath the Valu Fa Ridge, Lau Basin. *Journal of Geophysical Research*, *97*, 14,031–14,053. https://doi.org/10.1029/91JB02751

Crisp, J. A. (1984). Rates of magma emplacement and volcanic output. *Journal of Volcanology and Geothermal Research*, *20*(3–4), 177–211. https://doi.org/10.1016/0377-0273(84)90039-8

Davis, E. E., & Lister, C. R. B. (1977). Heat flow measured over the Juan de Fuca Ridge: Evidence for widespread hydrothermal circulation in a highly heat transportive crust. *Journal of Geophysical Research*, *82*, 4845–4860. https://doi.org/10.1029/JB082i030p04845

Davis, E. E., & Villinger, H. (1992). Tectonic and thermal structure of the Middle Valley sedimented rift, northern Juan de Fuca Ridge. *Proceedings Ocean Drilling Program, Science*, *139*(2), 9–41. https://doi.org/10.2973/odp.proc.ir.139.102.1992

DeMets, C., Gordon, R. G., & Argus, D. F. (2010). Geologically current plate motions. *Geophysical Journal International*, *181*(1), 1–80. https://doi.org/10.1111/j.1365-246X.2009.04491.x

Detrick, R. S., Buhl, P., Vera, E. E., Mutter, J., Orcutt, J. A., Madsen, J., & Brocher, T. (1987). Multi-channel seismic imaging of a crustal magma chamber along the East Pacific rise. *Nature*, *326*(6108), 35–41. https://doi.org/10.1038/326035a0

Dunn, R. A., Lekić, V., Detrick, R. S., & Toomey, D. R. (2005). Three-dimensional seismic structure of the Mid-Atlantic Ridge (35°N): Evidence for focused melt supply and lower crustal dike injection. *Journal of Geophysical Research*, *110*, B09101. https://doi.org/10.1029/2004JB003473

Dunn, R. A., Martinez, F., & Conder, J. A. (2013). Crustal construction and magma chamber properties along the Eastern Lau Spreading Center. *Earth and Planetary Science Letters*, *371–372*, 112–124.

Dunn, R. A., Toomey, D. R., & Solomon, S. C. (2000). Three-dimensional seismic structure and physical properties of the crust and shallow mantle beneath the East Pacific Rise at 9°30′N. *Journal of Geophysical Research*, *105*, 23,537–23,555. https://doi.org/10.1029/2000JB900210

Dziak, R. P. (2006). Explorer deformation zone: Evidence of a large shear zone and reorganization of the Pacific-Juan de Fuca-North American triple junction. *Geology*, *34*(3), 213–216. https://doi.org/10.1130/G22164.1

Francheteau, J., & Ballard, R. D. (1983). The East Pacific rise near 21°N, 13°N and 20°S: Inferences for along-strike variability of axial processes of the Mid-Ocean Ridge. *Earth and Planetary Science Letters*, *64*(1), 93–116. https://doi.org/10.1016/0012-821X(83)90055-9

Goss, A. R., Perfit, M. R., Ridley, W. I., Rubin, K. H., Kamenov, G. D., Soule, S. A., Fundis, A., et al. (2010). Geochemistry of lavas from the 2005-2006 eruption at the East Pacific Rise, 9°46′N-9°56′N: Implications for ridge crest plumbing and decadal changes in magma chamber compositions. *Geochemistry, Geophysics, Geosystems*, *11*, Q05T09. https://doi.org/10.1029/2009GC002977

Gregory, R. T., & Taylor, H. P. (1981). An oxygen isotope profile in a section of Cretaceous oceanic crust, Samail Ophiolite, Oman: Evidence for δ18O buffering of the oceans by deep (>5 km) seawater-hydrothermal circulation at mid-ocean ridges. *Journal of Geophysical Research*, *86*, 2737–2755. https://doi.org/10.1029/JB086iB04p02737

Gripp, A. E., & Gordon, R. G. (2002). Young tracks of hotspots and current plate velocities. *Geophysical Journal International*, *150*(2), 321–361. https://doi.org/10.1046/j.1365-246X.2002.01627.x

Hasenclever, J., Theissen-Krah, S., Rüpke, L. H., Morgan, J. P., Iyer, K., Petersen, S., & Devey, C. W. (2014). Hybrid shallow on-axis and deep off-axis hydrothermal circulation at fast-spreading ridges. *Nature*, *508*(7497), 508–512. https://doi.org/10.1038/nature13174

Henstock, T. J., Woods, A. W., & White, R. S. (1993). The accretion of oceanic crust by episodic sill intrusion. *Journal of Geophysical Research*, *98*, 4143–4161. https://doi.org/10.1029/92JB02661

Hooft, E. E. E., Detrick, R. S., & Kent, G. M. (1997). Seismic structure and indicators of magma budget along the Southern East Pacific rise. *Journal of Geophysical Research*, *102*, 27,319–27,340. https://doi.org/10.1029/97JB02349

Hooft, E. E. E., Patel, H., Wilcock, W., Becker, K., Butterfield, D., Davis, E., et al. (2010). A seismic swarm and regional hydrothermal and hydrologic perturbations: The northern Endeavour segment, February 2005. *Geochemistry, Geophysics, Geosystems*, *11*, Q12015. https://doi.org/10.1029/2010GC003264

Isaak, D. G. (1992). High-temperature elasticity of iron-bearing olivines. *Journal of Geophysical Research*, *97*, 1871–1885. https://doi.org/10.1029/91JB02675

Jackson, I., Paterson, M. S., & Fitz Gerald, J. D. (1992). Seismic wave dispersion and attenuation in Aheim dunite: An experimental study. *Geophysical Journal International*, *108*(2), 517–534. https://doi.org/10.1111/j.1365-246X.1992.tb04633.x

Karato, S. (1993). Importance of anelasticity in the interpretation of seismic tomography. *Geophysical Research Letters*, *20*, 1623–1626. https://doi.org/10.1029/93GL01767

Karsten, J. L., Delaney, J. R., Rhodes, J. M., & Liias, R. A. (1990). Spatial and temporal evolution of magmatic systems beneath the Endeavour Segment, Juan de Fuca Ridge: Tectonic and petrologic constraints. *Journal of Geophysical Research*, *95*, 19,235–19,256. https://doi.org/10.1029/JB095iB12p19235

Karsten, J. L., Hammond, S. R., Davis, E. E., & Currie, R. G. (1986). Detailed geomorphology and neotectonics of the Endeavour Segment, Juan de Fuca Ridge: New results from Seabeam swath mapping. *Geological Society of America Bulletin*, *97*(2), 213–221. https://doi.org/10.1130/0016-7606(1986)97<213:DGANOT>2.0.CO;2

Kelley, D. S., Baross, J. A., & Delaney, J. R. (2002). Volcanoes, fluids, and life at mid-ocean ridge spreading centers. *Annual Review of Earth and Planetary Sciences*, *30*(1), 385–491. https://doi.org/10.1146/annurev.earth.30.091201.141331

Kelley, D. S., Carbotte, S., Caress, D., Clague, D., Delaney, J., Gill, J., et al. (2012). Endeavour Segment of the Juan de Fuca Ridge: One of the most remarkable places on earth. *Oceanography*, *25*(1), 44–61. https://doi.org/10.5670/oceanog.2012.03

Kellogg, J. (2011). Temporal and spatial variability of hydrothermal fluxes within a mid-ocean ridge segment (PhD thesis). University of Washington, Seattle, WA.

Kent, G. M., Harding, A. J., & Orcutt, J. A. (1993). Distribution of magma beneath the East Pacific Rise between the Clipperton Transform and the 9°17′N Deval from forward modeling of common depth point data. *Journal of Geophysical Research*, *98*, 13,945–13,969. https://doi.org/10.1029/93JB00705

Kent, G. M., Singh, S. C., Harding, A. J., Sinha, M. C., Orcutt, J. A., Barton, P. J., et al. (2000). Evidence from three-dimensional seismic reflectivity images for enhanced melt supply beneath mid-ocean-ridge discontinuities. *Nature*, *406*(6796), 614–618. https://doi.org/10.1038/35020543

Kim, E., Toomey, D. R., Hooft, E. E. E., Wilcock, W. S. D., Weekly, R. T., Lee, S.-M., & Kim, Y. H. (2019). Upper crustal Vp/Vs ratios at the Endeavour segment, Juan de Fuca Ridge, from joint inversion of P and S traveltimes: Implications for hydrothermal circulation. *Geochemistry, Geophysics, Geosystems*, *20*, 208–229. https://doi.org/10.1029/2018GC007921

Kleinrock, M. C., Tucholke, B. E., Lin, J., & Tivey, M. A. (1997). Fast rift propagation at a slow-spreading ridge. *Geology*, *25*(7), 639–642. https://doi.org/10.1130/0091-7613(1997)025<0639:FRPAAS>2.3.CO;2

Langmuir, C. H., Bender, J. F., & Batiza, R. (1986). Petrological and tectonic segmentation of the East Pacific rise, 5°30′-14°30′ N. *Nature*, *322*(6078), 422–429. https://doi.org/10.1038/322422a0

Macdonald, K. C., Fox, P. J., Perram, L. J., Eisen, M. F., Haymon, R. M., Miller, S. P., et al. (1988). A new view of the mid-ocean ridge from the behaviour of ridge-axis discontinuities. *Nature*, *335*(6187), 217–225. https://doi.org/10.1038/335217a0

Macdonald, K. C., Scheirer, D. S., & Carbotte, S. M. (1991). Mid-ocean ridges: Discontinuities, segments and giant cracks. *Science*, *253*(5023), 986–994. https://doi.org/10.1126/science.253.5023.986

Marjanović, M., Carbotte, S. M., Carton, H., Nedimović, M. R., Mutter, J. C., & Canales, J. P. (2014). A multi-sill magma plumbing system beneath the axis of the East Pacific Rise. *Nature Geoscience*, *7*(11), 825–829. https://doi.org/10.1038/ngeo2272

Marjanović, M., Carbotte, S. M., Nedimovi, M. R., & Canales, J. P. (2011). Gravity and seismic study of crustal structure along the Juan de Fuca Ridge axis and across pseudofaults on the ridge flanks. *Geochemistry, Geophysics, Geosystems*, *12*, Q05008. https://doi.org/10.1029/2010GC003439

Mavko, G. M. (1980). Velocity and attenuation in partially molten rocks. *Journal of Geophysical Research*, *85*, 5173–5189. https://doi.org/10.1029/JB085iB10p05173

Morgan, J. V., Warner, M., Arnoux, G., Hooft, E., Toomey, D., VanderBeek, B., & Wilcock, W. (2016). Next-generation seismic experiments—II: Wide-angle, multi-azimuth, 3-D, full-waveform inversion of sparse field data. *Geophysical Journal International*, *204*(2), 1342–1363. https://doi.org/10.1093/gji/ggv513

Nicolas, A., Boudier, F., & Ildefonse, B. (1996). Variable crustal thickness in the Oman ophiolite: Implication for oceanic crust. *Journal of Geophysical Research*, *101*, 17,941–17,950. https://doi.org/10.1029/96JB00195

Schmeling, H. (1985). Numerical models on the influence of partial melt on elastic, anelastic and electric properties of rocks. Part I: Elasticity and anelasticity. *Physics of the Earth and Planetary Interiors*, *41*(1), 34–57. https://doi.org/10.1016/0031-9201(85)90100-1

Schouten, H., Klitgord, K. D., & Whitehead, J. A. (1985). Segmentation of mid-ocean ridges. *Nature*, *317*(6034), 225–229. https://doi.org/10.1038/317225a0

Seher, T., Crawford, W. C., Singh, S. C., Cannat, M., Combier, V., & Dusunur, D. (2010). Crustal velocity structure of the Lucky Strike segment of the Mid-Atlantic Ridge at 37°N from seismic refraction measurements. *Journal of Geophysical Research*, *115*, B03103. https://doi.org/10.1029/2009JB006650

Shaw, P. R., & Orcutt, J. A. (1985). Waveform inversion of seismic refraction data and applications to young Pacific crust. *Geophysical Journal International*, *82*(3), 375–414. https://doi.org/10.1111/j.1365-246X.1985.tb05143.x

Shoberg, T., Stein, S., & Karsten, J. (1991). Constraints on rift propagation history at the Cobb Offset, Juan de Fuca ridge, from numerical modeling of tectonic fabric. *Tectonophysics*, *197*(2–4), 295–308. https://doi.org/10.1016/0040-1951(91)90047-V

Sinton, J. M., & Detrick, R. S. (1992). Mid-ocean ridge magma chambers. *Journal of Geophysical Research*, *97*, 197–216. https://doi.org/10.1029/91JB02508

Soule, D., Wilcock, W. S. D., Toomey, D. R., Hooft, E. E. E., & Weekly, R. T. (2016). Near-axis crustal structure and thickness of the Endeavour Segment, Juan de Fuca ridge. *Geophysical Research Letters*, *43*, 5688–5695. https://doi.org/10.1002/2016GL068182

Sparks, D. W., & Parmentier, E. M. (1991). Melt extraction from the mantle beneath spreading centers. *Earth and Planetary Science Letters*, *105*(4), 368–377. https://doi.org/10.1016/0012-821X(91)90178-K
Toomey, D. R., & Foulger, G. R. (1989). Tomographic inversion of local earthquake data from the Hengill-Grensdalur Central Volcano Complex, Iceland. *Journal of Geophysical Research*, *94*, 17,497–17,510. https://doi.org/10.1029/JB094iB12p17497
Toomey, D. R., & Hooft, E. E. E. (2008). Mantle upwelling, magmatic differentiation, and the meaning of axial depth at fast-spreading ridges. *Geology*, *36*(9), 679–682. https://doi.org/10.1130/G24834A.1
Toomey, D. R., Jousselin, D., Dunn, R. A., Wilcock, W. S. D., & Detrick, R. S. (2007). Skew of mantle upwelling beneath the East Pacific Rise governs segmentation. *Nature*, *446*(7134), 409–414. https://doi.org/10.1038/nature05679
Toomey, D. R., Purdy, G. M., Solomon, S. C., & Wilcock, W. S. D. (1990). The three-dimensional seismic velocity structure of the East Pacific Rise near latitude 9°30′N. *Nature*, *347*(6294), 639–645. https://doi.org/10.1038/347639a0
Toomey, D. R., Solomon, S. C., & Purdy, G. M. (1994). Tomographic imaging of the shallow crustal structure of the East Pacific Rise at 9°30′ N. *Journal of Geophysical Research*, *99*, 24,135–24,157. https://doi.org/10.1029/94JB01942
Turner, I. M., Peirce, C., & Sinha, M. C. (1999). Seismic imaging of the axial region of the Valu Fa Ridge, Lau Basin—The accretionary processes of an intermediate back-arc spreading ridge. *Geophysical Journal International*, *138*(2), 495–519. https://doi.org/10.1046/j.1365-246X.1999.00883.x
Van Ark, E. M., Detrick, R. S., Canales, J. P., Carbotte, S. M., Harding, A. J., Kent, G. M., et al. (2007). Seismic structure of the Endeavour Segment, Juan de Fuca Ridge: Correlations with seismicity and hydrothermal activity. *Journal of Geophysical Research*, 112, B02401. https://doi.org/10.1029/2005JB004210
VanderBeek, B. P., Toomey, D. R., Hooft, E. E. E., & Wilcock, W. S. D. (2016). Segmentation of mid-ocean ridges attributed to oblique mantle divergence. *Nature Geoscience*, *9*(8), 636–642. https://doi.org/10.1038/ngeo2745
Weekly, R. T., Wilcock, W. S. D., Hooft, E. E. E., Toomey, D. R., McGill, P. R., & Stakes, D. S. (2013). Termination of a 6 year ridge-spreading event observed using a seafloor seismic network on the Endeavour Segment, Juan de Fuca ridge. *Geochemistry, Geophysics, Geosystems*, *14*, 1375–1398. https://doi.org/10.1002/ggge.20105
Weekly, R. T., Wilcock, W. S. D., Toomey, D. R., Hooft, E. E. E., & Kim, E. (2014). Upper crustal seismic structure of the Endeavour segment, Juan de Fuca Ridge from traveltime tomography: Implications for oceanic crustal accretion. *Geochemistry, Geophysics, Geosystems*, *15*, 1296–1315. https://doi.org/10.1002/2013GC005159
West, M., Menke, W., Tolstoy, M., Webb, S., & Sohn, R. (2001). Magma storage beneath Axial volcano on the Juan de Fuca mid-ocean ridge. *Nature*, *413*(6858), 833–836. https://doi.org/10.1038/35101581
White, S. M., Haymon, R. M., Fornari, D. J., Perfit, M. R., & Macdonald, K. C. (2002). Correlation between volcanic and tectonic segmentation of fast-spreading ridges: Evidence from volcanic structures and lava flow morphology on the East Pacific Rise at 9°–10°N. *Journal of Geophysical Research*, *107*(B8), 2173. https://doi.org/10.1029/2001JB000571
White, S. M., Macdonald, K. C., & Haymon, R. M. (2000). Basaltic lava domes, lava lakes, and volcanic segmentation on the southern East Pacific Rise. *Journal of Geophysical Research*, *105*, 23,519–23,536. https://doi.org/10.1029/2000JB900248
Whitehead, J. A., Dick, H. J. B., & Schouten, H. (1984). A mechanism for magmatic accretion under spreading centres. *Nature*, *312*(5990), 146–148. https://doi.org/10.1038/312146a0
Wilcock, W. S. D., Dougherty, M. E., Solomon, S. C., Purdy, G. M., & Toomey, D. R. (1993). Seismic propagation across the East Pacific Rise: Finite difference experiments and implications for seismic tomography. *Journal of Geophysical Research*, *98*, 19,913–19,932. https://doi.org/10.1029/93JB01820
Wilcock, W. S. D., Hooft, E. E. E., Toomey, D. R., McGill, P. R., Barclay, A. H., Stakes, D. S., & Ramirez, T. M. (2009). The role of magma injection in localizing black-smoker activity. *Nature Geoscience*, *2*(7), 509–513. https://doi.org/10.1038/ngeo550
Wilcock, W. S. D., Solomon, S. C., Purdy, G. M., & Toomey, D. R. (1995). Seismic attenuation structure of the East Pacific rise near 9°30′N. *Journal of Geophysical Research*, *100*, 24,147–24,165. https://doi.org/10.1029/95JB02280
Wilson, D. S. (1988). Tectonic history of the Juan de Fuca ridge over the last 40 million years. *Journal of Geophysical Research*, *93*, 11,863–11,876. https://doi.org/10.1029/JB093iB10p11863
Wilson, D. S. (1993). Confidence intervals for motion and deformation of the Juan de Fuca Plate. *Journal of Geophysical Research*, *98*, 16,053–16,071. https://doi.org/10.1029/93JB01227